Computational Fluid Dynamics Analysis in Support of the NASA/Virginia Tech Turbulence Model Validation Experiments

Colton T. Beardsley

Thesis submitted to the Faculty of the
Virginia Polytechnic Institute and State University
in partial fulfillment of the requirements for the degree of

Master of Science
in
Aerospace Engineering

Christopher J. Roy, Chair
Kevin T. Lowe
William J. Devenport

May 22, 2020
Blacksburg, Virginia

Keywords: Aerodynamics, Turbulence Modeling, CFD, Validation Experiments

Computational Fluid Dynamics Analysis in Support of the NASA/Virginia Tech Turbulence Model Validation Experiments

Colton T. Beardsley

(ABSTRACT)

Computational fluid dynamics methods have seen an increasing role in aerodynamic analysis since their first implementation. However, there are several major limitations is these methods of analysis, especially in the area of modeling separated flow. There exists a large demand for high-fidelity experimental data for turbulence modeling validation. Virginia Tech has joined NASA in a cooperative project to design and perform an experiment in the Virginia Tech Stability Wind Tunnel with the purpose of providing a benchmark set of data for the turbulence modeling community for the flow over a three-dimensional bump. This process requires thorough risk mitigation and analysis of potential flow sensitivities. The current study investigates several aspects of the experimental design through the use of several computational fluid dynamics codes.

An emphasis is given to boundary condition matching and uncertainty quantification, as well as sensitivities of the flow features to Reynolds number and inflow conditions. Solutions are computed for two different RANS turbulence models, using two different finite-volume CFD codes. Boundary layer inflow parameters are studied as well as pressure and skin friction distribution on the bump surface. The shape and extent of separation are compared for the various solutions. Pressure distributions are compared to available experimental data for two different Reynolds numbers.

Many aspects of this work were sponsored by NASA's Transformational Tools and Technologies Project. I gratefully acknowledge the support provided by NASA through an NRA award, grant 80NSSC18M0146.

Computational Fluid Dynamics Analysis in Support of the NASA/Virginia Tech Turbulence Model Validation Experiments

Colton T. Beardsley

(GENERAL AUDIENCE ABSTRACT)

Computational fluid dynamics (CFD) methods have seen an increasing role in engineering analysis since their first implementation. However, there are several major limitations is these methods of analysis, especially in the area of modeling of several common aerodynamic phenomena such as flow separation. This motivates the need for high fidelity experimental data to be used for validating computational models. This study is meant to support the design of an experiment being cooperatively developed by NASA and Virginia Tech to provide validation data for turbulence modeling. Computational tools can be used in the experimental design process to mitigate potential experimental risks, investigate flow sensitivities, and inform decisions about instrumentation. Here, we will use CFD solutions to identify risks associated with the current experimental design and investigate their sensitivity to incoming flow conditions and Reynolds number. Numerical error estimation and uncertainty quantification is performed. A method for matching experimental inflow conditions is proposed, validated, and implemented. CFD data is also compared to experimental data. Comparisons are also made between different models and solvers.

Dedication

To my loving wife, Anna, and to my family who have supported me in every area during my time as a student

Acknowledgments

I would like to thank Dr. Christopher Roy for his helpful insight and consistent feedback on my work. His teaching and advising helped me to direct my work in the right direction and to create more meaningful data.

I would like to thank Dr. Todd Lowe and Dr. William Devenport for serving on my committee. Their challenging questions and research knowledge helped me to think critically about the work that I do and motivated me to do it well.

I would like to thank the student members of the project team who helped to contribute to this work in a variety of ways and provided mutual support. This includes Aldo Gargiulo, Julie Duetsch, Vidya Vishwanathan, and Daniel Fritsche. They exemplified what it means to be good team members and contributed to my learning and overall experience as a graduate student.

I would like to thank Weicheng Xue for his willingness to help me in troubleshooting issues that I frequently ran into with computational fluid dynamics programs.

I would like to thank my church members at Providence Presbyterian Church in Christiansburg for caring for me and my wife during my time as a graduate student and providing me with a community to lean on.

I would like to thank my wife, Anna Beardsley, for her constant care and support as well as sacrifices she has made to allow me to pursue this path.

Contents

List of Figures

List of Tables

Chapter 1

Introduction

1.1 Motivation

The NASA/Virginia Tech Turbulence Model Validation Experiments are a set of experiments being designed and performed at Virginia Tech with input and collaboration from NASA Langley Research Center. The goal of the study is to obtain a set of benchmark data to be used for validating a variety of turbulence models. This project includes multiple risk reduction studies and entries in the stability wind tunnel. An emphasis is given to experimental uncertainty quantification and boundary condition documentation. The geometry chosen is a novel three-dimensional bump geometry.

The solutions are first obtained using the computational fluid dynamics (CFD) solver under development at Virginia Tech. The Structured Euler/Navier-Stokes Explicit/Implicit solver (SENSEI) [1] is used to obtain many solutions. CFD investigations have proven useful in areas where experimental studies are either too expensive or infeasible. The objective of the CFD analysis is to provide a computational study of the bump geometry mounted in the Virginia Tech Stability Wind Tunnel for the purpose of providing insight into the experimental design by investigating flow sensitivities and identify potential design risks.

An investigation with CFD identifies an area of separation on the bump's windward face and then proceeds to study this feature as it behaves at different Reynolds numbers and boundary conditions. The sensitivity of the flow to both the size and uniformity of the boundary layer is also explored to ensure repeatability of the experiments. Another advantage of using CFD is the ability to obtain all variables at all locations in the flow field. Obtaining volumetric data through experimental measurements is both difficult and costly. It is necessary to obtain this information to characterize the flow in different regions and give insight into decisions on where and how to collect experimental measurements.

1.2 Outline

The first chapter of this work provides the motivation for the NASA/Virginia Tech Benchmark Experiments as well as general background on model validation experiments. The second chapter includes all of the computational methodology and analyses performed to support the design of these experiments. The third chapter discusses the conclusions that are drawn from this analysis and identifies areas for future computational study of this case.

1.3 Contribution

A method of automatic mesh generation for the flow of a three-dimensional bump in a wind tunnel is created. An alternate computational geometry for boundary layer matching at the inflow of the stability wind tunnel is proposed. Quantification of iterative and discretization errors in the numerical simulations is performed. Sensitivity of the flow over the bump to incoming boundary layer size and asymmetry is investigated. Solutions for the flow field are obtained using both SENSEI and Fluent with both Spalart-Allmaras k-ω turbulence models. Reynolds number effects are also studied and identified.

1.4 Attribution

Due to the manuscript format of this thesis, Chapter 2 is attributed to multiple authors. A brief summary of the contributions of each author to this work is given here:

- Colton T. Beardsley (First Author): The first author was the primary author and contributed the majority of the content. The first author generated all computational domains and domain discretizations. The first author ran and processed data for boundary layer sensitivity studies cases as well as for solver and model sensitivities. The first author also performed all of the solution analysis for the study of Reynolds number effects. The first author performed code verification and solution verification with error estimation.
- Aldo Gargiulo (Second Author): The second author contributed the obtaining of solutions for some cases pertaining to error estimation. The second author also assisted in obtaining experimental pressure data and oil flow images for the bump geometry in the stability wind tunnel.
- Thomas Ozoroski (Third Author): The third author obtained solutions in SENSEI for the study of Reynolds number effects for the bump flow.

- Julie Duetsch-Patel (Fourth Author): The fourth author contributed much of the experimental pressure data as well as the processing of the this data.
- Vidya Vishwanathan (Fifth Author): The fifth author assisted in obtained data from experiments in the Stability Wind Tunnel.
- Daniel J. Fritsch (Sixth Author): The sixth author assisted in obtained data from experiments in the Stability Wind Tunnel.
- Máté Szöke (Seventh Author): The seventh author assisted in obtained data from experiments in the Stability Wind Tunnel. The seventh author also gave valuable feedback and contributed suggestions that influenced the results obtained.
- Aurelien Borgolts (Eighth Author): The eighth author contributed valuable feedback and suggestions that influenced the quality of the results obtained.
- Kevin T. Lowe (Ninth Author): The eighth author contributed valuable feedback and suggestions that influenced the results obatined.
- Christopher Roy (Tenth Author): The ninth author served as the main advisor to the direction of the computational studies perfomed and therefore contributed to the results obtained
- William J. Devenport (Eleventh Author): The eighth author contributed valuable feedback and suggestions that influenced the quality of the results obtained.

Chapter 2

CFD Analysis for Assessment of Experimental Design Risks and Flow Sensitivities

Colton T. Beardsley[1], Aldo Gargiulo[2], Thomas Ozoroski [3], Vidya Vishwanathan[2], Daniel J. Fritsch[2], Julie E. Duetsch-Patel[2], Máté Szöke[4], Aurelien Borgoltz[5], Kevin T. Lowe[6], Christopher J. Roy[7], William J. Devenport[6]

2.1 Introduction

The NASA/Virginia Tech Benchmark Experiments for Computational Fluid Dynamics (CFD) Validation are a set of experiments performed in Virginia Tech's Stability Wind Tunnel to study the flow over a three-dimensional bump. The goal of the experiments is to meet the highest demands of CFD validation as defined by Oberkamp and Smith [2]. This includes rigorous uncertainty quantification, experimental design configuration, and extensive documentation of the boundary conditions of the flow and their sensitivities. This effort is

[1]Graduate Researcher, Kevin T. Crofton Department of Aerospace and Ocean Engineering, Student Member.

[2]Graduate Research Assistant, Kevin T. Crofton Department of Aerospace and Ocean Engineering, Student Member.

[3]Undergraduate Researcher, Kevin T. Crofton Department of Aerospace and Ocean Engineering.

[4]Postdoctoral Researcher, Kevin T. Crofton Department of Aerospace and Ocean Engineering, Member.

[5]Research Associate Professor, Kevin T. Crofton Department of Aerospace and Ocean Engineering, Member.

[6]Associate Professor,Kevin T. Crofton Department of Aerospace and Ocean Engineering, Associate Member.

[7]Professor, Kevin T. Crofton Department of Aerospace and Ocean Engineering, Associate Fellow.

being made over a three-year period from 2018-2021, including several experiments of varying scales for risk-reduction. This study aims to provide as much information as possible for use in setting up and running CFD simulations. The flow over a bump has been studied at other institutions but not with this level of focus on uncertainty quantification. Previous studies have often assumed the value of a particular boundary condition or fail to document the geometry as it is built as opposed to the theoretical, designed geometry. When these assumptions are made, corresponding uncertainties are propagated throughout the entire computational model, thus motivating a collaborative effort between experimentalists and CFD researchers to ensure that the experiment meets rigorous standards of uncertainty quantification [3].

Turbulence model validation is an area of great concern to the aviation community as designers have strong incentive to use predictive CFD tools for critical design decisions. This may include attempting to certify air vehicles through computational analysis, thereby reducing the costs associated with wind tunnel or flight testing and certification. Other safety applications include load prediction on wind turbine blades operating in the atmospheric boundary layer. Successful and feasible turbulence modeling techniques are required to accurately simulate these types of flow. To determine the success of a particular modeling approach, experimental data for a variety of flow conditions must be known within an acknowledged uncertainty level. Furthermore, for comparisons with experimental data to be made appropriately, boundary conditions of the flow must be known within a documented uncertainty to provide the specified boundary conditions of the computational model. The sensitivities of the flow to said boundary conditions are of high concern.

The study of aerodynamic bump flows has been of particular interest to the computational community for a variety of reasons. First, this flow provides several turbulent flow features that pose challenges for computational analysis methods. As the flow approaches the wall-mounted bump, a two-dimensional boundary layer becomes highly accelerated and skewed. The flow then separates over the leeward side of the bump before reattaching on the wall downstream. The current design features a smooth geometry so that the location of the separation and reattachment locations may be used as a metric of model fidelity. In addition to being a challenge to computationalists, the flow is well-suited for CFD validation test cases. The inflow condition is a two-dimensional boundary layer plane flow, which is simple to model and well-understood. Three-dimensional bumps may also be designed with geometry symmetry, with the intention of providing symmetry checks that can be used for error identification. It should be noted here that creating a symmetric geometry does not guarantee a symmetric flow field as may be evidenced by results in this study. A third advantage of the three-dimensional bump geometry is the lack of interaction between the separated flow regions and the sidewall boundary layers, thus contributing to modeling simplicity and feasibility of boundary condition documentation.

An effort of this scale requires predictive tools to inform design decisions. Here, the advantage of CFD tools is twofold. A computational fluid dynamics study of the flow provides predictive flow data for geometries and conditions that are not able to be studied experimentally due to

physical restrictions or expense. Furthermore, these solutions provide flow data through the entire domain. This allows the team to utilize CFD to model flows at varying scales and with varying geometries and boundary conditions to identify potential risks and flow behaviors under various conditions. Like experimental data, computational data requires a rigorous quantification of uncertainties. Here, grid convergence studies are performed, CFD solvers are compared, boundary condition sensitivities are analyzed, and wind tunnel geometry is considered.

2.2 Approach

2.2.1 Flow Conditions

Here is studied the aerodynamic flow past a three-dimensional, wall-mounted bump in the Stability Wind Tunnel. Characteristics of the flow have been chosen to achieve high Reynolds number results. The flow velocity is set near 55 m/s in the test section, with an average free-stream air density of 1.1272 kg/m^3. The ambient temperature during experiments has been measure to be 286 K which corresponds to a dynamic viscosity of the fluid being approximately 1.78e-5 Pa-s according to Sutherland's law. The Reynolds number in this case is calculated based upon the height of the bump geometry and is approximately 650k. The mach number for this flow is approximately .162. Compressibility effects are taken into account by all CFD codes to obtain corresponding solutions. Results are also obtained for a flow speed of 27.5 m/s corresponding to a Reynolds number of 325k and a freestream Mach number of .0801.

2.2.2 Geometry

The geometries relevant to the flow may be considered in two general categories: the geometry of the bump model that is to be mounted on the wind tunnel wall, and the geometry of the wind tunnel. Here, a distinction must be made between the geometries as they are designed theoretically and how they are built. Initial runs are made with the assumption of equivalence between as-designed and as-built geometries. Runs are also made to analyze the sensitivity in certain quantities due to differences from the idealized geometry. Studies are planned to quantify the differences between as-designed and as-built geometries that allow for CFD studies of these differences as well.

The Stability Wind Tunnel is a closed-circuit, low-speed tunnel used for commercial, research, and educational aerodynamic testing purposes. The primary concern of the current study is the test section of the tunnel in which the bump geometry is mounted and the contraction as shown in Figure 2.1. The test section is 7.3 m long with a 1.85 m square cross section. Solutions are obtained for the flow within this portion of the wind tunnel. To match the

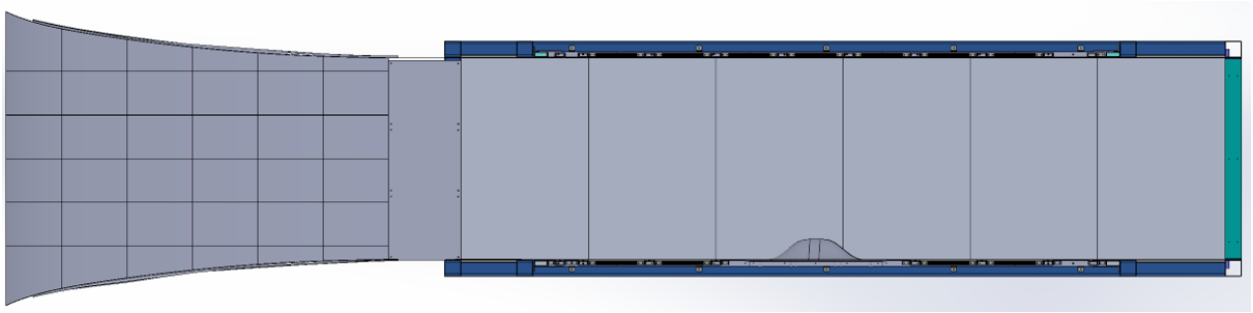

Figure 2.1: The as-designed geometry of the contraction and test section.

inflow conditions in the test section, one may consider a variety of strategies including the modeling of the contraction geometry. This requires the measurement of the contraction geometry via a laser scanner and subsequent processing. A more thorough computational study of the Stability Wind Tunnel was performed for uncertainty quantification by Szöke, et al [4]. We will not consider this complex of a method here but rather choose to extrude the inlet face of the test section upstream by a certain distance to allow the boundary layer to develop until it matches the conditions measured in the test section. A full discussion of boundary layer matching at the test section inflow will be given in a later section.

The bump geometry for this study is novel and analytic. It is generated using a fifth degree polynomial curve to ensure continuous curvature in every dimension. The bump geometry also incorporates a flat upper section and is flat on all surrounding sides. The four sides have a continuous curvature around the corners by using a 4^{th}-order super-ellipse. The details of the bump can be seen in Figure 2.2. Continuous curvature allows for the use of separation and reattachment locations as a metric of modeling fidelity for validation studies. The geometry is suited for three-dimensional validation studies due to the interest of validating three-dimensional modeling techniques or implementations [5].

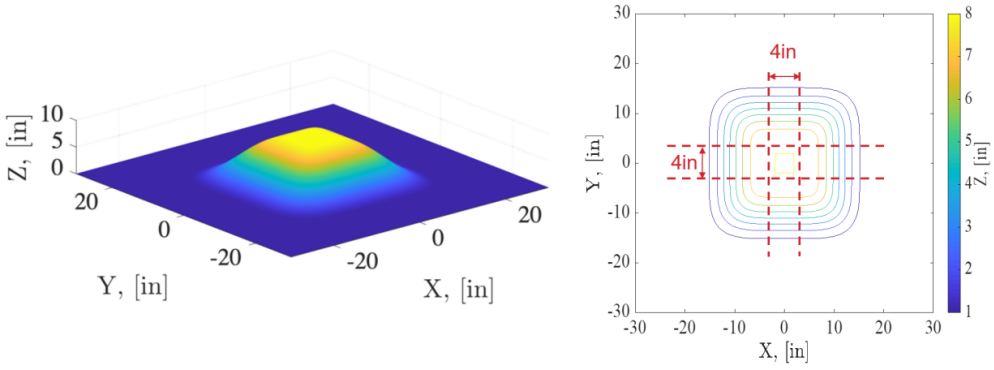

Figure 2.2: Designed geometry of the three-dimensional bump.

2.2.3 Numerical Grid

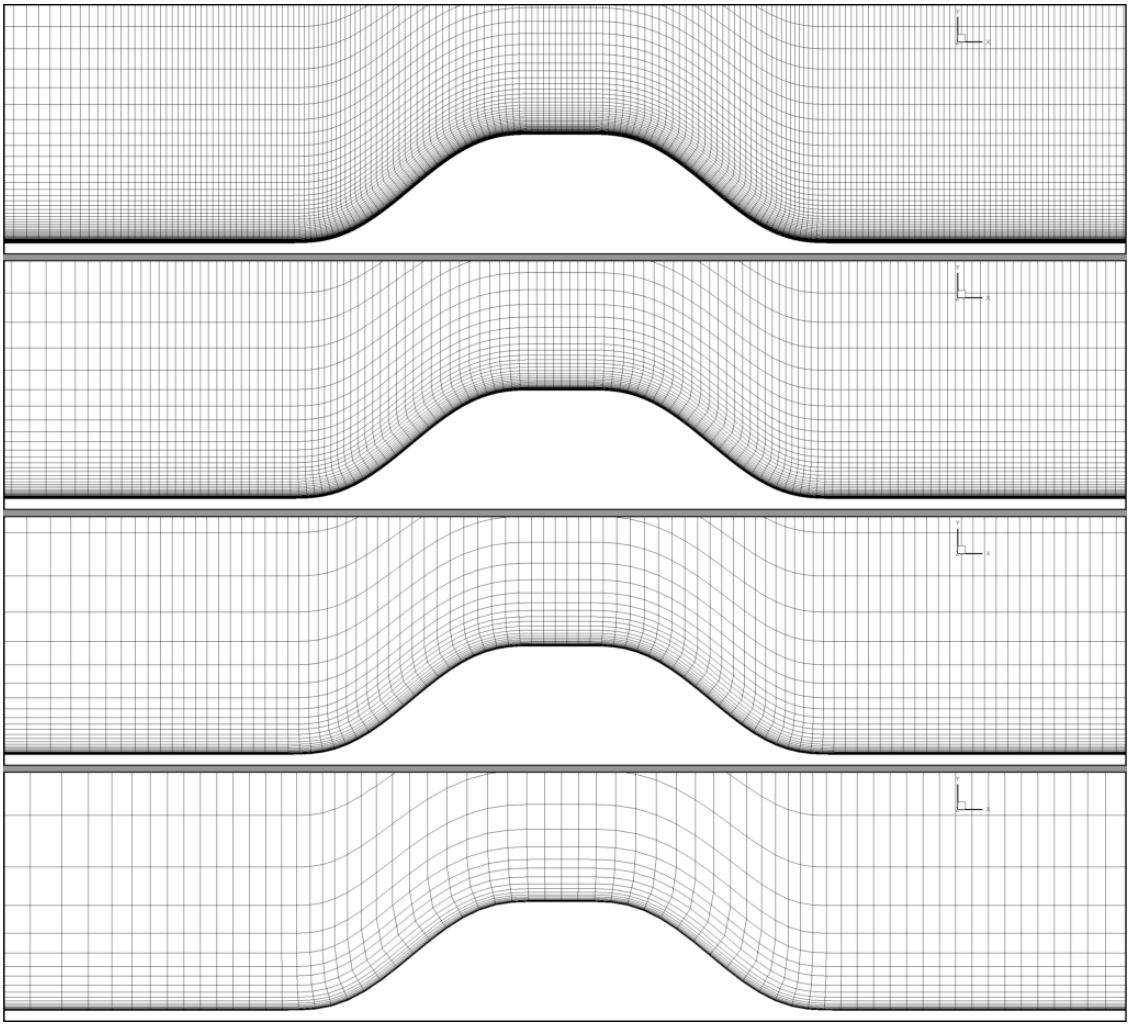

Figure 2.3: A plane taken at the mid-span of the bump showing the mesh in this region with grid level 0 (Top) through through grid level 3 (Bottom)

Once the computational domain is specified, the volume must be discretized. A family of four grids is generated for the purpose of discretization error estimation. A non-integer coarsening factor is used to obtain four systematically refined grids. Typical coarsening scripts that allow for non-integer coarsening require some interpolation and thereby incur some error in the geometry produced. To avoid introducing error into the computational geometry, a method of automated mesh generation implemented in the mesh generation software, Pointwise. Here, a generic script is developed to generate a mesh for the specified geometry. This script may then be altered to change the dimensions and spacings of different regions of the mesh. With a selected coarsening factor, the spacings may be multiplied by the coarsening factor and the dimensions may divided by the coarsening factor to result in a

newly generated mesh that has been systematically coarsened. Done consistently, the result of multiple automatically generated meshes is a family of systematically coarsened grids with an arbitrary coarsening factor. The coarsening factor chosen here is $\sqrt{2}$. For the sake of convenience in nomenclature, the finest mesh level is considered as mesh level 0, and each subsequent coarsening produces another grid level, resulting in grid levels 1, 2, and 3, with grid level 3 being the coarsest. This is the terminology that will be used for the remainder of the study. The resulting family of grids can be visualized by a cut plane taken at the midspan of the bump in Figure 2.3.

To verify the implementation of this method, scripts are generated for grid level 2 with two different strategies for comparison. First, grid level 0 was generated and then coarsened by removing every other grid point in each of the three grid dimensions. This is provides a traditional approach for coarsening that is assumed to be consistent and systematic. Grid level 2 was then generated again using the automatic mesh generation tool. It was seen that the grid topology has changed only very slightly and that the difference in solutions is indistinguishable. This is therefore considered to be a successful method of generating a systematically coarsened family of grids.

This family of grids is produced with grid lines being everywhere normal to each of the tunnel surfaces. First, a rectangular grid is produced by specifying an increased concentration of cells both spanwise and streamwise in the region of the bump. This rectangular grid is then projected linearly onto the bump geometry and wall where it is then extruded normally outward. The resulting surface grid is shown in Figure 2.4. The rest of the domain is then built around this region of interest where the grid spacing grows as the indexing moves away from the bump. Grid spacing is specified as .001 mm at each of the four walls of the tunnel on the finest grid and is therefore .00282 mm on the coarsest grid to properly resolve the boundary layer in this region for wall-resolved, RANS turbulence modeling with wall y^+ values below one.

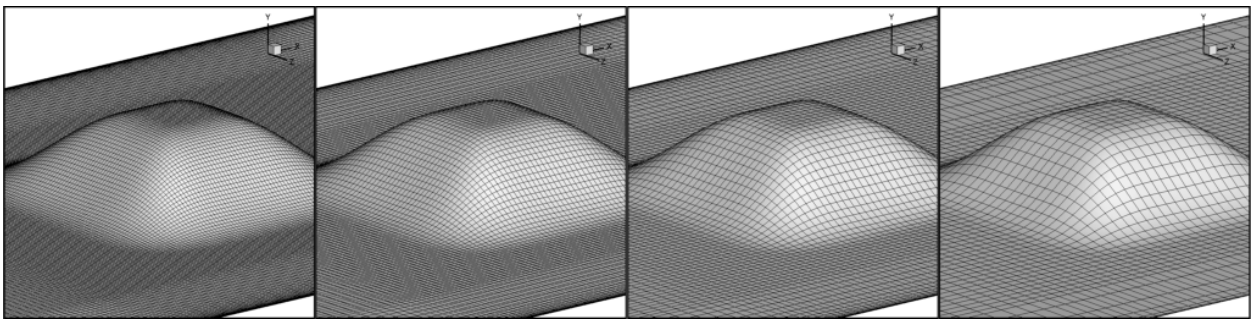

Figure 2.4: The mesh on the bump surface is shown for each mesh level. Four meshes are generated for the geometry.

An added benefit of implementing this system of automatic mesh generation is the time saved in meshing new geometries, or making slight changes to the spacing in different regions. As is true in many CFD studies, the current grids used to obtain the results in this study are a

product of several iterations of mesh design. Creating a script to generate such grids increases efficiency in iterating over the grid design substantially. This specific script also includes the benefit of meshing different geometries quickly and similarly due to the method of mesh generation. By specifying a different geometry, the scripts simply projects the surface mesh onto the new geometry and performs the normal extrusion from the surface mesh in the same way as for the original geometry. This method allows for efficient generation of new geometries while maintaining similar grid spacing and topology. This allows for comparisons of solutions for different model geometries. Such geometric studies are not performed here but will be performed in the future of the NASA/Virginia Tech Benchmark Experiments project.

2.2.4 Modeling Approach

To model the flow, Reynolds-Average Navier-Stokes (RANS) solvers are used. Unless otherwise specified all solutions are obtained from the use of a Structured Euler Navier-Stokes Explicit Implicit Solver (SENSEI), a research code under development at Virginia Tech [6] [1]. Solutions are also obtained with ANSYS Fluent v18 to make comparisons between codes and their results. Both codes are run using the compressible, Reynolds-Averaged, Navier-Stokes equations with finite volume discretizations. A second-order spatial discretization is used in each case. Cases are run in SENSEI using primarily the Spalart-Allmaras turbulence model [7], but solutions are obtained for comparison using the Menter k-ω SST model as well [8]. Each model's implementation in SENSEI has undergone successful order-of-accuracy code verification by Xue et. al. [9]. In this case, the two-equation model is initialized by the solution using the one-equation model.

2.2.5 Boundary Conditions

A large challenge of the current study is to specify appropriate and accurate boundary conditions for direct comparison with the validation experiments. The walls of the tunnel, including the bump, are all modeled as no-slip walls, while pressures are used to model the inlet and outlet boundary conditions. At the inlet, the stagnation pressure is specified as 94300 to match measurements done at the Stability Wind Tunnel. At the outlet, the pressure is adjusted to approximately match the desired Reynolds number. The full-scale target Reynolds number of the experiments is 650k, based on the bump height as the characteristic length. Experimental data has also been obtained for a Reynolds number of 325k. Compressible flow theory is used to calculate the approximate outlet pressure to produce the desired free-stream velocity without accounting for stagnation pressure loss throughout the domain. The true free-stream pressure in the solution is taken from an average of x-component velocity values across multiple cells centered on the inlet face. As mentioned previously, an extrusion of the inflow plane upstream is used to properly match the inflow boundary layer

as measured in corresponding experiments. The outlet face is specified to lie 5m downstream of the bump mid-chord to avoid influence of the specifications here. It is assumed that the downstream geometry of the wind tunnel has negligible impact on the flow in the regions of interest, and therefore these features are not considered in the computational domain.

2.3 Verification and Uncertainty Quantification

2.3.1 SENSEI Code Verification

SENSEI was used to obtain many solutions for this case. The code was run implicit in pseudo-time with a second order discretization scheme in space. Because the Spalart-Allmaras turbulence model is used, the code solves a system of six differential equations. To gain confidence in the implementation of discretization schemes and algorithms implemented, the method of manufactured solutions is used to verify the solver. Here, we repeat the case performed by Jackson et. al. [1] using the method of manufactured solutions. The selected solution is one of a three-dimensional cross-sinusoidal variation of each of the variables in space. The form of the solution is given in Equation 2.1. Constants are specified to ensure subsonic flow, and their specific values can be found in the Appendix. The domain is also sinusoidal in all three dimensions. The volume is discretized uniformly in all directions.

$$\begin{aligned} f = {} & a_1 + a_2 sin(a_3 \pi x/l + a_4 \pi) + a_5 sin(a_6 \pi y/l + a_7 \pi) \\ & + a_8 sin(a_9 \pi z/l + a_{10} \pi) + a_{11} sin(a_{12} \pi xy/l^2 + a_{13} \pi) \\ & + a_{14} sin(a_{15} \pi yz/l^2 + a_{16} \pi) + a_{17} sin(a_{18} \pi xz/l^2 + a_{19} \pi) \end{aligned} \tag{2.1}$$

This solution is then entered into the governing equations and corresponding source terms are solved for to satisfy the equations. Implementing the source term into the solver then allows us to generate solutions for the manufactured case. Solutions are generated on five different grid levels to allow for the evaluation of four observed orders of accuracy. This choice was made for several reasons. A convenient coarsening factor of two in each of the three direction allows for successful convergence of 5 different grid levels within a reasonable time frame. This also gives confidence that the finest grids will be in the asymptotic range. Finally, it allows one to see the general trend of the observed order of accuracy to give confidence that the finest grid levels are indeed in the asymptotic range. The grid levels chosen have 128, 64, 32, 16, and 8 computational cells in each spatial dimension. An example of a computational solution is shown in Figure 2.5.

The discretization error is then calculated according to its definition as the difference between the discrete solution and exact solution. The L_1, L_2, and L_∞ norms can then be taken of the discretization errors for each cell for each of the dependent variables. A plot of the results is given in Figure 2.6. The formal order slope is also plotted alongside the results for

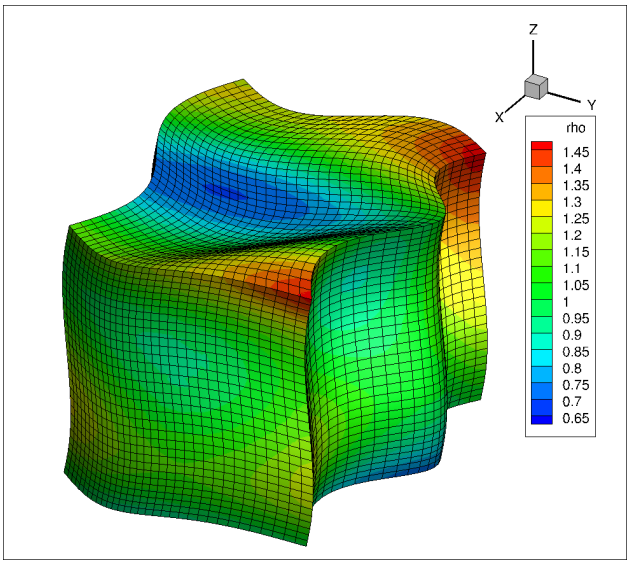

Figure 2.5: Manufactured solution calculated for 32 grid cell mesh

comparison. Because the scheme is second order accurate, we should see the errors in the solution reduce with the square of the grid spacing. It should be noted that this assumption is only valid for solutions within the asymptotic region.

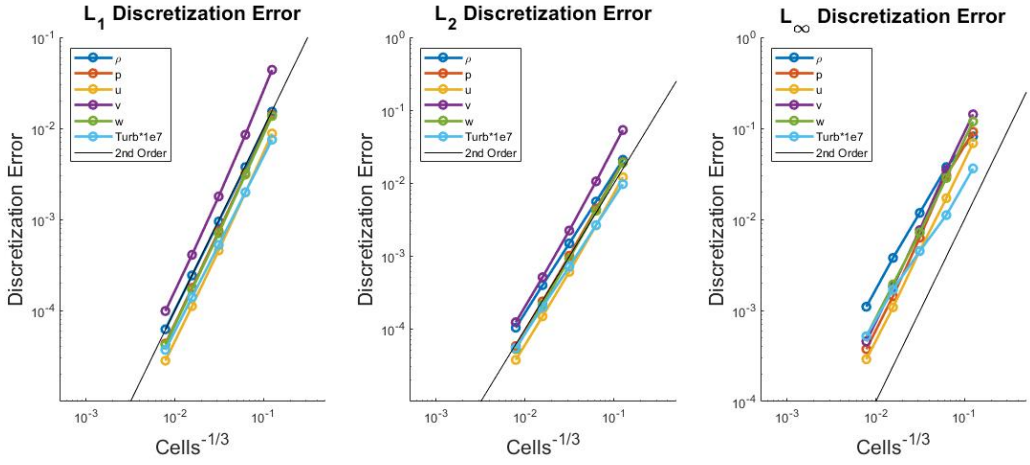

Figure 2.6: Three norms of discretization error for manufactured solution

From the discretization error on each mesh level, we are able to calculate an observed order of accuracy, $\hat{p}$ via equation 2.2, using the discretization errors from a fine mesh level, DE_h and the next coarsest mesh level, DE_{rh}, as well as the grid refinement factor, r. For this case the grid refinement factor is two, and we should expect that the observed order of accuracy closely match the formal order of two for the finest grid levels.

$$\hat{p} = \frac{log(DE_h - DE_{rh})}{log(r)} \tag{2.2}$$

Using five mesh levels allows for the calculation of four observed orders of accuracy. These are plotted as a function of grid spacing in Figure 2.7. In these plots, we see clearly that for each of the norms used, the observed order of accuracy generally converges very near to the formal order for the finest grid levels. This is an indication that these grid levels are indeed in the asymptotic range, lending validity to the order or accuracy calculation here. This also indicates that the schemes are accurately implemented and that the algorithms chosen are well-suited for solving the discrete equations. It should be noted that the behaviour of the L_∞ norms is less uniform than the others. The nature of this norm is that it only depends on a single, local value. Therefore, it is prone to less predictive behaviour. We may then conclude that the L_1 and L_2 norms provide a better indication for how the solution behaves overall with grid refinement.

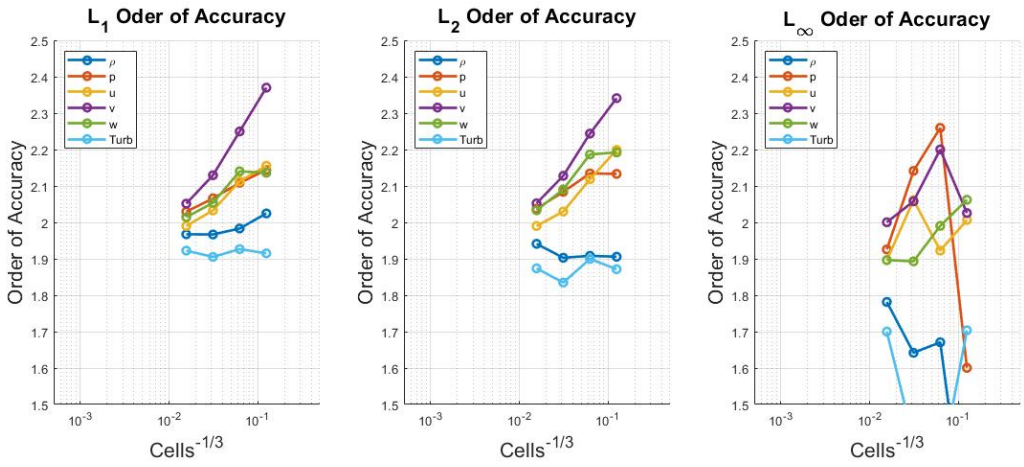

Figure 2.7: Observed order of accuracy from manufactured solution

2.3.2 Iterative Error Estimation

Iterative error ε_h^k can be generally defined as the difference between the current approximate iterative solution u_h^k of an iterative solution method for the discretized PDEs and the exact solution u_h of the discretized PDE. Here, we will assume that round-off errors are negligible in comparison with iterative and discretization errors and are therefore not considered. This assumption is justified by the fact that all computations are run in double precision.

$$\varepsilon_h^k = u_h^k - u_h \tag{2.3}$$

We can mathematically express the discretized PDEs of the problem using a discretization operator L such that $L(u_h) = 0$.

The iterative solution of the discretized PDE at a particular iteration k, however, only satisfy latter equation up to a residual R. We can then write this residual as in Equation 2.4.

$$L(u_h^k) = R(u_h^k) \tag{2.4}$$

As the iteration number tends toward infinity, the residual value eventually stops decreasing due to the effect of finite-precision computing. As the residuals continue to decrease, round-off errors eventually result in the inability of the iterative solution method to continue improving the solution. At this point, the iterative residual is assumed to be small enough that it is generally negligible. An example of the residual history for which this behaviour is exhibited is given in Figure 2.8. Here we see residual convergence into the round-off region at the 17000^{th} iteration for grid level 3.

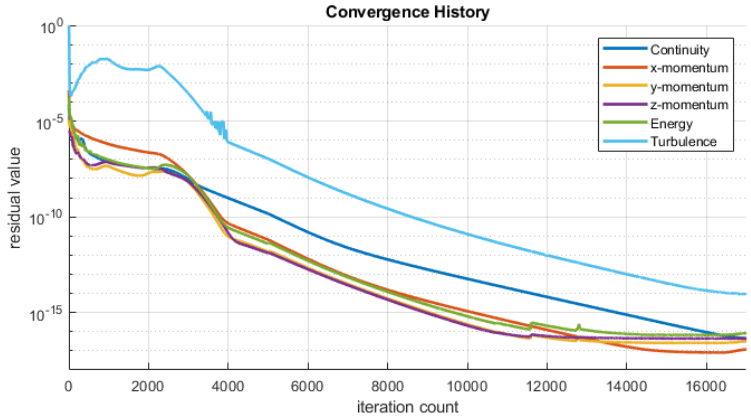

Figure 2.8: Iterative residuals for the coarsest mesh level

To approximate the iterative error, we use the solution at the final iteration as an approximation of the exact solution to the discrete equations and estimate the iterative error in the solution saved at several previous iterations according to Equation 2.3. We will first consider the error in the pressure development over the windward face of the bump. The gauge pressure is taken relative to a point upstream of the bump center by 1.82 m and on the opposite wall to correspond with carefully chosen pressure taps present during corresponding experiments. This gauge pressure is then normalized by the freestream dynamic pressure taken from velocity and density values at the cells along inlet face. An array of pressure coefficients along the center line is extracted from the solution at each time step and the error relative to the last time steps is calculated. The L_∞ norm of this error array is then taken as a conservative indication of the magnitude of error. This can them be plotted along with the residuals as a function of the iteration number to show how the iterative error behaves

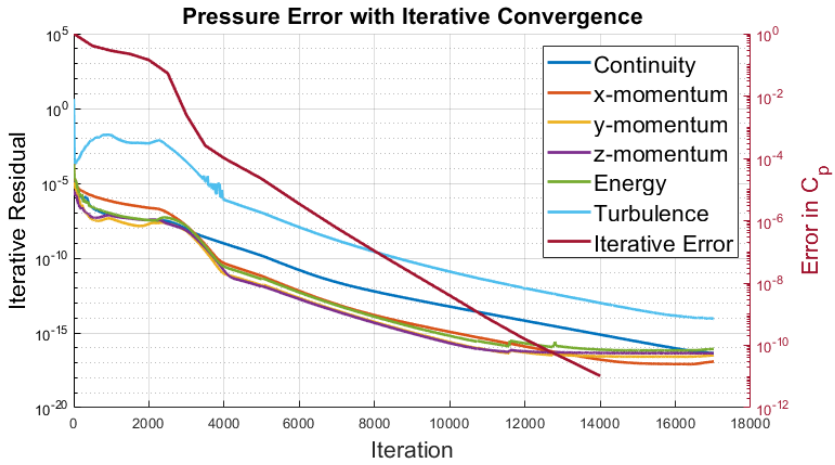

Figure 2.9: Iterative error in pressure along the center line

throughout convergence. The residual history with iterative error estimation is plotted in Figure 2.9.

Rather than running every solution into this round-off region, we choose to put a bound on the iterative error and develop a corresponding criteria for the residuals of the mean flow and turbulence equations. This allows for much shorter computing times as subsequent solutions may only be run for the number of iterations required to meet this error restriction with the understanding that the estimated iterative. To ensure that there exists a reasonably small amount of error in this value, we require that the error in the pressure coefficient be less than 1e-3. This is satisfied by the 4000^{th} iteration where the maximum error in pressure is 1.01e-4. From this, we can derive a criteria for the value of the iterative residuals to ensure that the iterative error remains below this value. We may notice that the values for the residuals for the turbulence and mean flow equations have slightly different behaviour with a large difference in their magnitudes. This encourages us to develope seperate criteria for the mean flow and turbulence equations. At the 4000^{th} iteration, the turbulence residual value is 9.52e-7 and the maximum residual for the mean flow equations is 9.52e-10. Therefore, for future runs we use these two values as respective criteria for turbulence and mean flow residuals to ensure low errors in the surface pressure.

We may also consider the system response quantity of shear stress along the center line of the bump. This is done in the same way as for the pressure coefficient as is seen in Figure 2.10. Here, the shear stress is normalized by the freestream dynamic pressure to yield the skin friction coefficient.

At the iteration required for convergence of the pressure coefficient on the bump, the error in the predicted skin friction coefficient is 6.95e-7 and is therefore within an acceptable range. Therefore, we are encouraged to maintain the criteria based upon the error in pressure with the knowledge that this results in an estimated error in the skin friction coefficient of 6.95e-7.

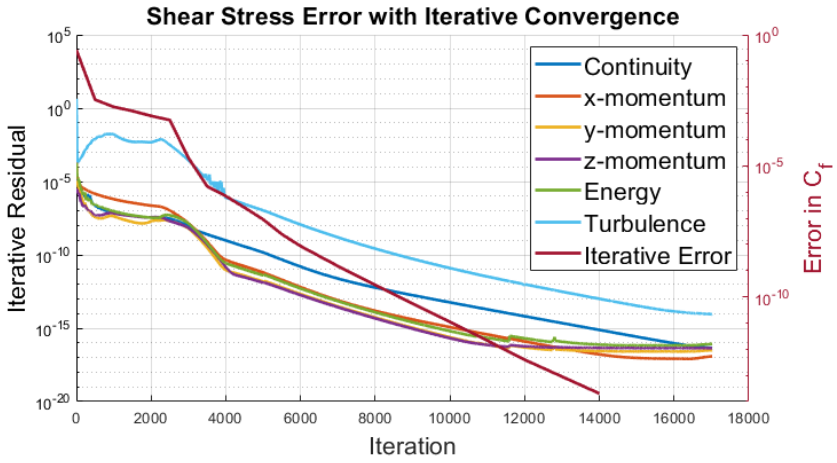

Figure 2.10: Iterative error in pressure along the center line

2.3.3 Discretization Error

Discretization is the error due to approximations made in the discretization process and is therefore the difference between the exact solution to the analytic PDEs and the discrete equations. Estimating this value is complex as the exact solution to analytic equations is not available, nor is the exact solution to the discrete equations. To approximate the discretization error, the solution to the discrete equations is treated as an estimate of the exact solution to the discrete equation for that mesh level. This assumes that both round-off and iterative errors are significantly smaller than the discretization error on the fine grid. Estimates of iterative error from the previous section serve to prove that the iterative error is very small for sufficiently converged cases. Round-off error is assumed to be small as well because all computations are performed in double precision.

Because an exact solution is not known, the process used here is Richardson extrapolation [10]. Richardson extrapolation uses solutions of several mesh levels to extrapolate to a higher-order solution. This higher-order solution may then serve as an approximation of the exact solution to the analytic equations for the purpose of estimating the discretization error. For these cases, the leading term of the truncation error is a function of the square of the grid spacing such that the formal order, p, is two. Using solutions on the grid level 0, f_0, and grid level 1, f_1, with the grid refinement factor, r an estimate of the exact solution, $\bar{f}_h$, is calculated according to Equation 2.5.

$$\bar{f}_h = f_0 + \frac{f_0 - f_1}{r^p - 1} \tag{2.5}$$

From this estimation of the exact solution, the discretization error on each mesh level is estimated. As with the iterative error estimation, we first consider the pressure on the center line of the windward side of the bump. The pressures here are extracted as an array for each

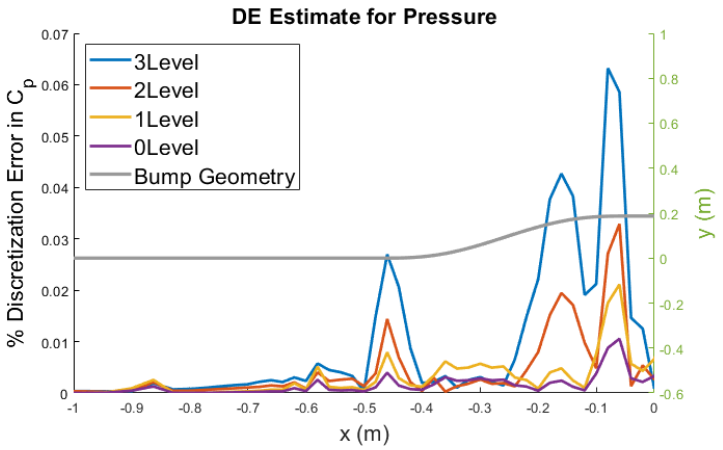

Figure 2.11: Discretization error in pressure coefficient on center line of the bump's windward face

mesh level. Because of the implementation of a non-integer coarsening factor, these data are not co-located. To account for this, a cubic spline interpolation is used to interpolate to the coarsest level. Because the order of this interpolation is higher than that of the solution itself, we can have confidence that the errors incurred in the interpolation process will have negligible impact on the analysis. The Richardson extrapolation is performed for each of the data points and the discretization error in the pressures are then simply computed as the difference in the extrapolated values and the solution values on each mesh level. The results of this analysis are given in Figure 2.11.

In the discretization error of pressures approaching the bump, we see that the coarsest grid has relatively high error, as one might expect. The maximum value for the discretization error in the pressure coefficient on grid level three is about .066. Similar to the approach with the iterative error, these discrete errors may be treated as methods by which to determine appropriate grid spacing for future cases. On grid level two, the maximum discretization error in the pressure coefficient is .029. This provides sufficient approximation for use in sensitivity study as to not incur the high computational cost for running many cases on the finer level grids. The finest grid has a maximum discretization error of .011 in the pressure coefficient in this region. Because the solution has already been obtained on this grid level for this study, it will be used to compare to experimental data with the distribution of the associated discretization error estimates being reported.

The same analysis may be done for the shear stress distribution along the center line on the bump's leeward face. The shear stress coefficient is obtained by using a finite difference approximation for the derivative of velocity in the wall-normal direction at the face of each cell using a stencil that extends two cells above the surface. This also takes advantage of the fact that the value at the face is zero due to the wall boundary condition that has been specified here. Therefore, a three-point stencil can be constructed to calculate this value

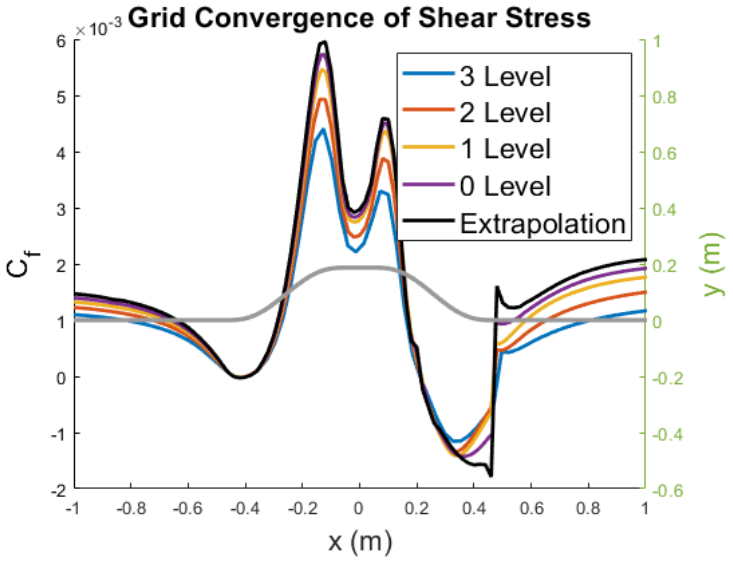

Figure 2.12: Shear stress distribution for every mesh level and extrapolated solution

with second order accuracy. Because the accuracy of this method is of the same order of the Richardson extrapolation, the errors incurred in the calculation of the shear stress coefficient is assumed to not influence this method.

The value of shear stress in this region is important as it indicates where the flow separates and how it behaves within the region of separation. Again, an array of values for the shear stress are obtained along the center line for each of the four meshes and are then interpolated using a cubic spline method to the location of the coarse grid points. The shear stress distribution is plotted in Figure 2.12. One may notice a general convergence to the extrapolated solution in most regions with the exception of the reattached region. It is clear that different mesh levels result in different predictions of reattachment. This influences the results of this method in this region behind the bump.

The discretization error is estimated for the shear stress by taking the difference between the solutions on each mesh level and the extrapolated solution. Results for this are plotted on the leeward side of the bump in Figure 2.13.

We see that the discretization error in the shear stress coefficient is very large for the region where the shear stress peaks as the flow accelerates over the curvature at the top of the bump, just prior to separation. In other areas, the discretization error is not as high. We therefore conclude that though the error in shear stress is high for grid level 2, it is still within an acceptable range for use in studies of flow sensitivity.

One of the most important assumptions of the methodology that we have employed here is that the grids that we are running on are within the asymptotic range. This is the range where the leading term of the truncation error sufficiently dominates the contribution of the

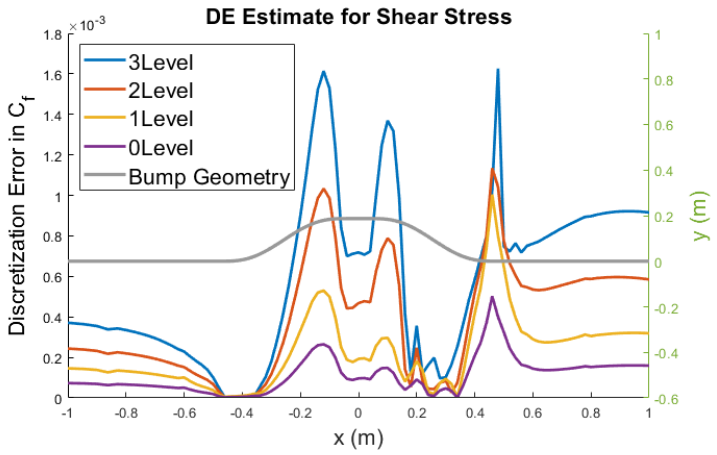

Figure 2.13: Shear stress distribution for every mesh level and extrapolated solution

trailing terms. If the solutions are indeed in the asymptotic range, then the difference in the predicted solution should converge with grid refinement according to the formal order of accuracy of the scheme. To test whether this is true, we can compute an observed order of accuracy according to Equation 2.6.

$$OOA_{observed} = \frac{log(\frac{f_2 - f_1}{f_1 - f_0})}{log(r)} \tag{2.6}$$

Because this study has used four mesh levels, two observed orders of accuracy may be computed: one for grid level one and one for grid level zero. The solution parameters that are used to calculate the observed order of accuracy are the pressure along the center line of the windward face of the bump as well as the shear stress along the center line of the bump. Because these are both arrays, the L_2 norm is taken of the difference between mesh levels. The results of this calculation are given in Table 2.1.

Table 2.1: Observed orders of accuracy from grid convergence

	Grid Level 1	Grid Level 0
Pressure	1.892	1.931
Shear Stress	.544	1.129

We see here that the formal order of accuracy is approximately matched for the finest grid using the pressure data. The values here raise some question as to whether or not grid level three is within the asymptotic region. Even so, the extrapolation is based solely upon the finest two grid levels which gives confidence that the extrapolation performed is accurate and which supports the validity of the results from the pressure data. In contrast from

the solutions using the pressure data, the results from the shear stress data show that the grids do not display behaviour consistent with the formal order of accuracy. It is difficult to say why this occurs. It may be due to changes in the actual flow phenomena due to grid refinement. Further investigation is required to properly characterize the discretization errors in this region.

In addition to the discretization from Richardson extrapolation, the grid convergence index is calculated. This is a way of reporting uncertainties in discretization error set forward by Roache [11]. Here, a factor of safety, F_s is used along with the formal order of accuracy, p. The expression for Roache's grid convergence index is given in Equation 2.7.

$$GCI = \frac{F_s}{r^p - 1}|f_1 - f_0| \tag{2.7}$$

In this expression, the formal order or accuracy may be replaced with the observed order of accuracy when the observed order of accuracy is exhibits a difference of 10% or more from the formal order according to Oberkampf and Roy [10], and the values from the fine grid solution in the denominator omitted. It is also recommended that the observed order be limited to the formal order, and that the factor of safety be three for such cases and otherwise 1.25. Therefore, the grid convergence index is calculated using the formal order of accuracy with a factor of safety of 1.25 for the pressure and 3 for the shear stress. This provides a relatively conservative estimate for the uncertainty due to discretization error for both the pressure and shear stress coefficient values. The L_2 norm is taken of the difference between solutions to calculate the index. The grid convergence index for the pressure coefficient is calculated to produce an uncertainty of $\pm.001$, and similarly, the uncertainty in the shear stress coefficient is estimated to be ± 1.30 Pa.

The total numerical uncertainty can be calculated as the sum of uncertainties from the iterative errors and discrete errors, with the assumption that round-off errors provide a negligible contribution. We take the direct sum here as opposed to a root-sum-square approach which is more common for combining experimental uncertainties. This is because the root-sum-square combination assumes the independence of the errors as well as the random nature of them. In these computational solutions, these uncertainties are neither random nor independent, leading us to choose the more conservative approach of a direct summation for combining these numerical uncertainties. The uncertainty due to iterative error is given as the iterative error estimation, expressed as an interval about the true solution. Therefore the uncertainty in pressure due to iterative error is $\pm$ 1 Pa. Adding this to the uncertainty due to discretization error suggests a final uncertainty of $\pm$ 41.8 Pa. Similarly, we may express the uncertainty in the shear stress as $\pm$ .1282 Pa. Combining this with information from the discretization error, the total numerical uncertainty in the shear stress is estimated as 1.43 Pa.

2.4 Inflow Condition Matching and Sensitivity

2.4.1 Matching the Experimentally Measured Boundary Layer

As mentioned in the introduction section, upstream extrusion of the test section is chosen as the method by which the boundary layer at the inflow of the test section will be matched. The square inlet face of the computational domain is extruded upstream. The boundary layer is initialized at the inlet face and its thickness, displacement thickness, and momentum thickness are increased as one moves downstream of the inlet face. In order to directly compare CFD and experimental data, it must be ensured that boundary conditions between the computational and physical domains are consistent. Therefore, the goal of the following analysis is to generate an upstream inlet geometry that successfully matches results calculated from experimental data. The rake is mounted on each of several modular panels that make up the wall of the wind tunnel in this section. Figure 2.14 shows the modular design of the tunnel and the nomenclature used to refer to specific panels. Experimental data are collected on panels P3T, P3M, P3B, and P4M with the bump model mounted in the tunnel.

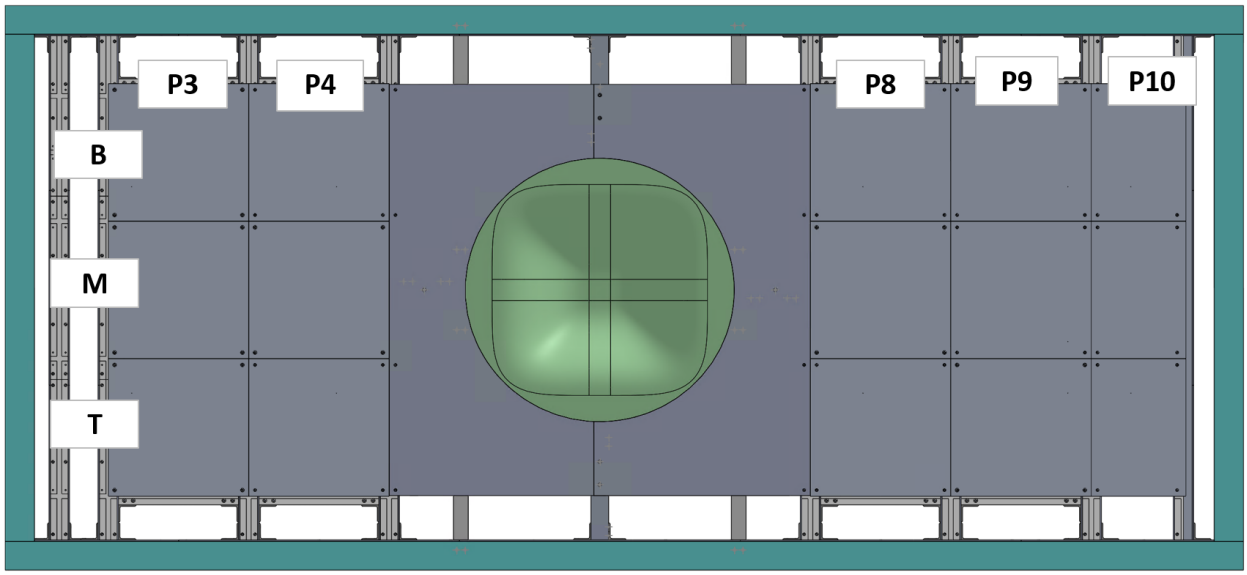

Figure 2.14: Modular panel nomenclature for the port wall of the stability wind tunnel

The boundary layer profile at these locations serve as the values that this study will attempt to match. To properly analyze this data, an interpolation must first be made for the profile near the wall. The closest probe to the wall on the rake does not supply data that is near enough to make accurate calculations of the boundary layer integral quantities and cannot provide wall shear measurements. To account for the important data that exist between the wall, where the velocity is zero, and the first probe location, a Spalding fit is employed. The Spalding boundary layer profile takes the form of Equation 2.8 [12]. Because the value u^+

depends on the wall shear value, the distance from there exist three unknown quantities: B, κ, and the wall shear.

$$y^+ = u^+ + e^{-\kappa B}(e^{\kappa u^+} - 1 - \kappa u^+ - \frac{1}{2!}(u^+)^2 - \frac{1}{3!}(u^+)^3) \tag{2.8}$$

Several of the probes closest to the wall are used to perform a least-squares regression fit of the form given by the Spalding fit. The resulting regression then gives the two shape variables and the wall shear stress for the boundary layer profile. Points between the wall and the first measured point are then evaluated. The resulting boundary layer profile on the P3M panel is shown in Figure 2.15. This method provides a full profile for the boundary layer obtained through the experiments.

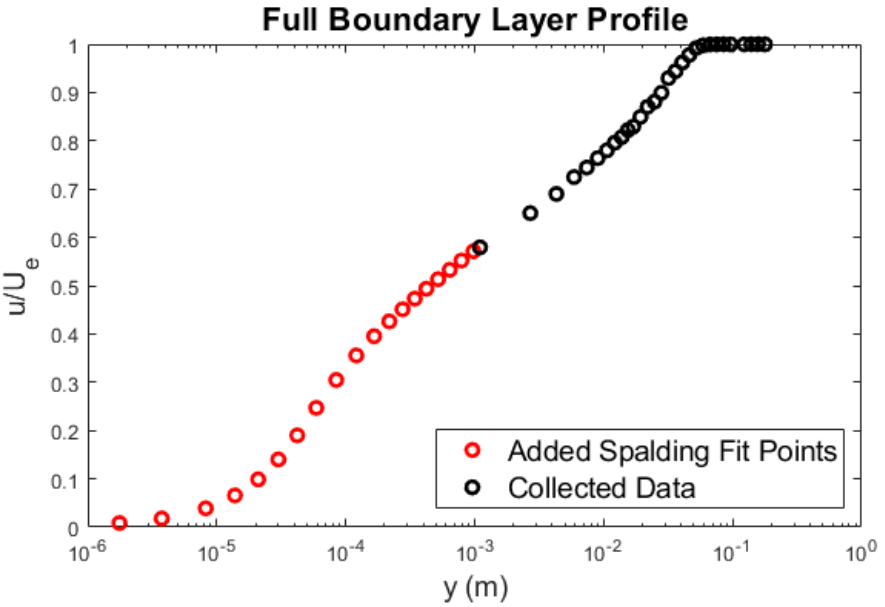

Figure 2.15: Experimental boundary layer with points added from Spalding fit

We now seek to match several of the integral boundary layer quantities. The displacement thickness of the boundary layer is given by Equation 2.9. Physically, this may be interpreted as the thickness by which the wall might displacement in a uniform flow field to produce the same mass flow as for the viscous boundary layer flow. It integrates a function of the flow velocity, u, over the boundary layer thickness, δ.

$$\delta^* = \int_0^\delta (1 - \frac{u}{U_e})dy \tag{2.9}$$

Similarly, the momentum thickness is physically the thickness by which the wall might displacement in a uniform flow field to produce the same momentum as for the viscous boundary layer flow. The expression for this value is given in Equation 2.10.

$$\theta = \int_0^{\delta} \frac{u}{U_e}(1 - \frac{u}{U_e})dy \tag{2.10}$$

These integral quantities may be approximated using the experimental data with the Spalding fit using a trapezoidal rule integration. The boundary layer thickness is defined here as the wall-normal location at which the velocity is 98% that of the edge velocity. The location where this value is met may also be interpolated from the experimental data. The result for each of the four panels is given in Table 2.2.

Table 2.2: Experimental boundary layer quantities

Panel	Thickness (mm)	Displacement Thickness (mm)	Momentum Thickness (mm)
P3B	42.23	5.803	4.516
P3M	46.73	6.880	5.294
P3T	52.13	7.707	5.917
P4M	51.29	7.573	5.885

To model the boundary layer at this point in the test section, several different extents of upstream extrusion are generated and solutions obtained. This cases are identified by the location of their inlet face relative to the bump's mid-chord location. Cases of 6.5 m, 6 m, 5.5 m, 5 m, and 4 m are considered. The boundary layer at the test section inlet is then taken from each of these solutions for comparison. Because of the physical importance of both momentum and displacement thickness, these are the values that are chosen for attempted matching of experimental and CFD inflow conditions. The boundary layers are taken at the P3M panel with the assumption of similarity for the results of the P3T and P3B panels from the CFD solutions. The quantities here are calculated in the same way as for the experimental data, with a trapezoidal rule for numerical integration. A curve is then fit to the data to provide a continuous function. A least-squares fitting is used, using the form given in Equation 2.11 where C_1, C_2, and C_3 are the constants solved for in the fitting process. The equation form is here written for the momentum thickness, θ, as a function of the inlet location relative to the bump, x_i, but the same form is also used for the displacement thickness.

$$\theta = C_1(x_i - C_3)^{C_2} \tag{2.11}$$

The resulting relationships for the displacement and momentum thickness are then retrieved from this analysis. These are plotted in Figure 2.16. It is seen that the curve fits give a relationship between the location of the inlet face and the boundary layer quantities at the test section inlet. This smooth function allows us to approximate the necessary location of the inlet to produce a corresponding boundary layer at the test section entrance.

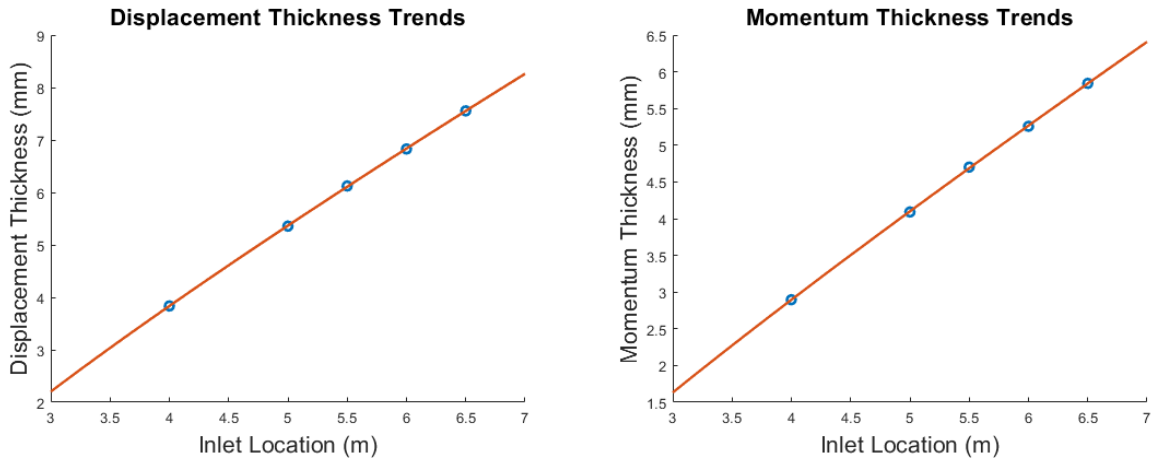

Figure 2.16: Displacement and momentum thickness at test section inlet for symmetric inflow CFD solutions

The curve fit is used to approximate the inlet location in order to match the momentum and displacement thicknesses at P3M, resulting in two inlet locations. To match the displacement thickness, it is estimated that the inlet needs to be 6.030 m upstream of the bump center, and to match the momentum thickness, it is estimated that the inlet needs to be 6.023 m upstream of the bump center. Both of these locations are very close to one another as well as to one of the symmetric inlet conditions already run. Therefore, we may consider the case for which the inlet face is placed 6 m upstream of the bump a sufficient solution to match the boundary layer at this location. The error in the displacement thickness at this station is .7525%, and the error in the momentum thickness at this station is .684%, proving the strong agreement between the CFD solution and experimental data for this geometry and at this location.

One may note that there exists a significant difference in the boundary layer values as measured in the experiments for difference span-wise stations, despite being at the same stream-wise location. This observation indicates an asymmetry in the inflow boundary layer due to effects of tunnel geometry that are not accounted for by the idealized domain. The spanwise nonuniformity of the boundary layer calls for the computational modeling of an asymmetric boundary layer inflow to obtain proper matching of boundary conditions. To accomplish this, the inlet of the test section is not extruded upstream asymmetrically. This results in an inlet that is no longer normal to the flow but at some slope. This allows the boundary layer to develop to different extents span-wise in the tunnel. The geometry of the inlet is determined using the analysis from the symmetric boundary layer solutions. At each span-wise station for which boundary layer data is measured, the test section is extruded upstream by a distance that is approximated by the fits performed in the previous section. In all cases, the approximation of inlet locations to match displacement and momentum thicknesses are very similar and so the average of the two values is taken with the intention of incurring minimal error in both values. A linear variation is then imposed between the

three span-wise stations which then also extends to the top and bottom walls of the test section. Because solutions for symmetric geometries exhibit asymmetry in the flow field, it is important that, not only this geometry, but also its mirror be analyzed to assess potential influences on the asymmetry of the flow field downstream. The meshes from the two resulting geometries are shown in Figure 2.17.

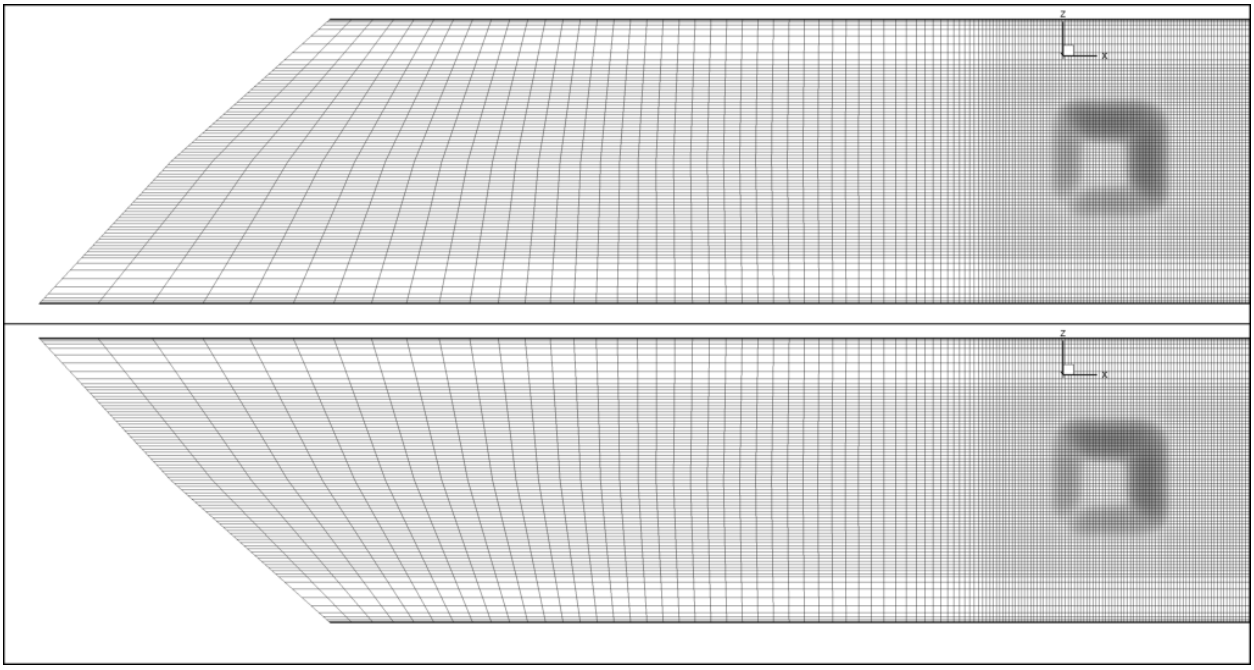

Figure 2.17: Asymmetric inlet geometries used to match inflow conditions

Each of these meshes is run and the boundary layers are retrieved at each span-wise station. A plot of the boundary layer profiles comparing the experimentally measure boundary layer profile with added near-wall data using Spalding fit and the profiles as predicted by the CFD solutions is given in Figure 2.18. We see that at each of the span-wise stations, the boundary layer profile seems to be of the same shape as the measured profile and generally has the same near-wall behaviour as the Spalding fit.

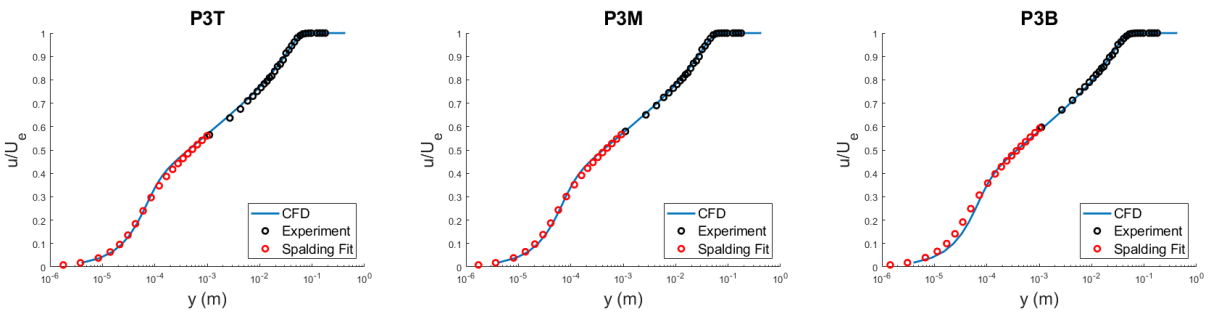

Figure 2.18: Asymmetric inlet geometries used to match inflow conditions

To assess the accuracy of this method, the integral values are calculated for each of the three panels in the CFD solutions. The percentage error as compared to the experimental data can then be calculated for both the displacement and momentum thickness. These values are tabulated in Table 2.3. The comparison shows that the error in the integral values is always below 1.5%. The solution obtained from this geometry is therefore assumed to be indicative of the boundary layer in the experiments performed and will generally be used for future solutions to ensure the matching of experimental boundary conditions.

Table 2.3: Error in CFD modeling of inflow boundary layer quantities

Panel	Displacement Thickness Error	Momentum Thickness Error
P3B	1.43%	.110%
P3M	.523%	.264%
P3T	.921%	.135%

2.4.2 Influence of Inflow on Bump Flow

We now turn our attention to the effects of the inflow geometry on the flow over the bump. Because there are multiple test sections that may be used in the stability wind tunnel, it is possible that the switching of test sections may result in slightly different inflow boundary layer characteristics. The tunnel walls are also modular which creates the potential of small changes of geometry when instrumentation is changed or panels are removed or replaced. If the flow over the bump is highly sensitivity to the inflow boundary layer, then these small changes in the tunnel would pose a huge risk to the repeatably of the wind tunnel experiments. The analysis of the sensitivity of the flow in the region of the bump to the boundary layer at the inlet of the test section is considered in two parts. The first part considers the extent to which the asymmetry in the boundary layer effects the flow over the bump surface. The second consideration is the overall size of the boundary layer as a potential influence. These analyses differ slightly in that the case for which the boundary layer is asymmetric may be compared directly to other cases with different span-wise characteristics but with the similar values of skin friction and displacement thickness as the flow approaches the bump. Alternatively, the size of the boundary layer has the potential to influence the freestream due to blockage in the tunnel. Different boundary layer sizes may also create different conditions for shear stress as the flow approaches the bump.

To consider the boundary layer asymmetry's effect on the bump, three cases are compared. The first is the standard case that was chosen to match the boundary layer of the experiments. The mirrored geometry which results in a mirrored boundary layer flow approaching the bump is also considered. The symmetric case for which the boundary layer is matched only at the middle panel of the test section is the last case considered and is assumed to produce a

symmetric boundary layer. Because the flow over the bump has been shown to be span-wise asymmetric, one might suspect that any asymmetry in the boundary layer flow may have influence over the direction or extent of the asymmetry in the wake region due to varying shears approaching the bump. The pressure distribution for the asymmetric geometry used to match the experimental boundary layer and its mirror are plotted in Figure 2.19. The results here show that the asymmetry of the boundary layer inflow has no influence over the direction of the asymmetry or its extent.

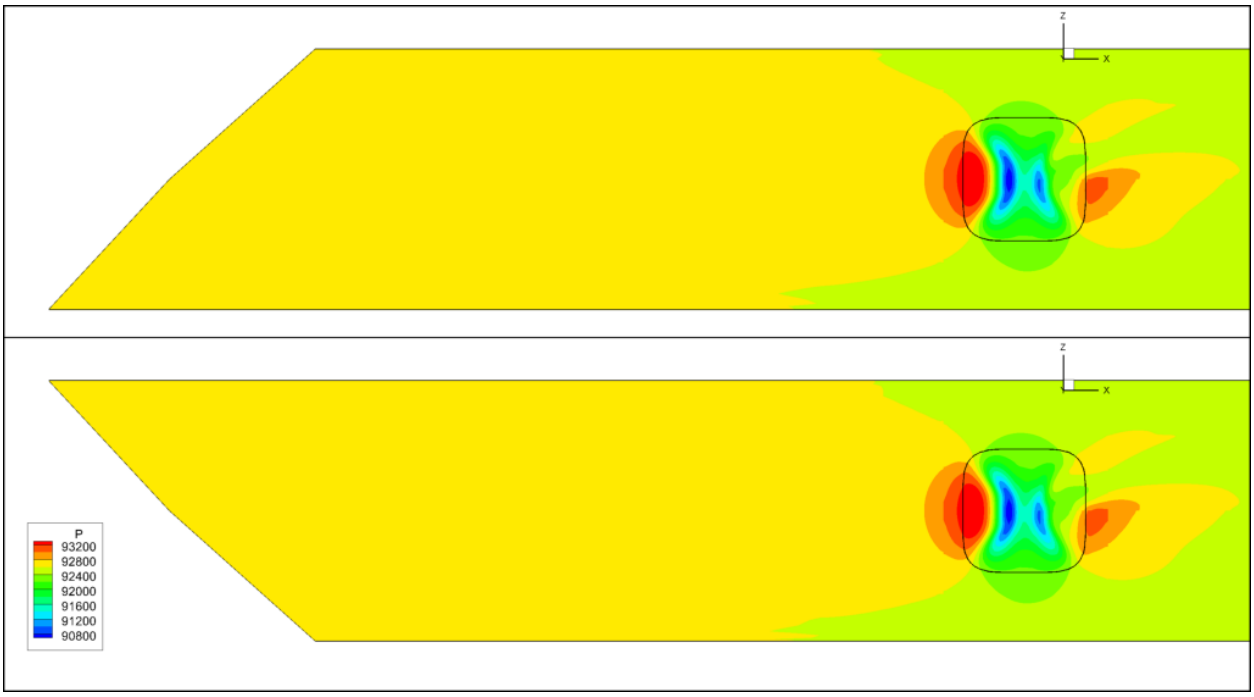

Figure 2.19: Pressure distribution for mirrored inflow geometries showing the wake asymmetry is insensitive to spanwise variations in the incoming boundary layer

Given that the asymmetry in the wake remains the same for each of the two asymmetric inflow geometries, we will now consider the pressure and shear distributions along the center line for each solution to give a quantitative comparison of potential influences in this region. The pressure and kin friction coefficient relative to the standard asymmetric case is plotted in Figure 2.20 for the bump region. It is important to note here the magnitudes on the y-axis of each of these plots as it is very small which suggests that the asymmetry in the incoming boundary layer has little or no effect on the shear of pressure over the bump. We will interpret this observation as an indication that the flow over the bump is not significantly altered by the asymmetry in the incoming boundary layer. It is hypothesized that the influence of the pressure gradient approaching the bump dominates the behaviour of the boundary layer in this region making the flow over the bump independent of upstream values of boundary layer quantities. It is recommended that computationalists who study this case in the future employ the standard asymmetric geometry generated here, but, where convenient, this may

be substituted with a symmetric geometry.

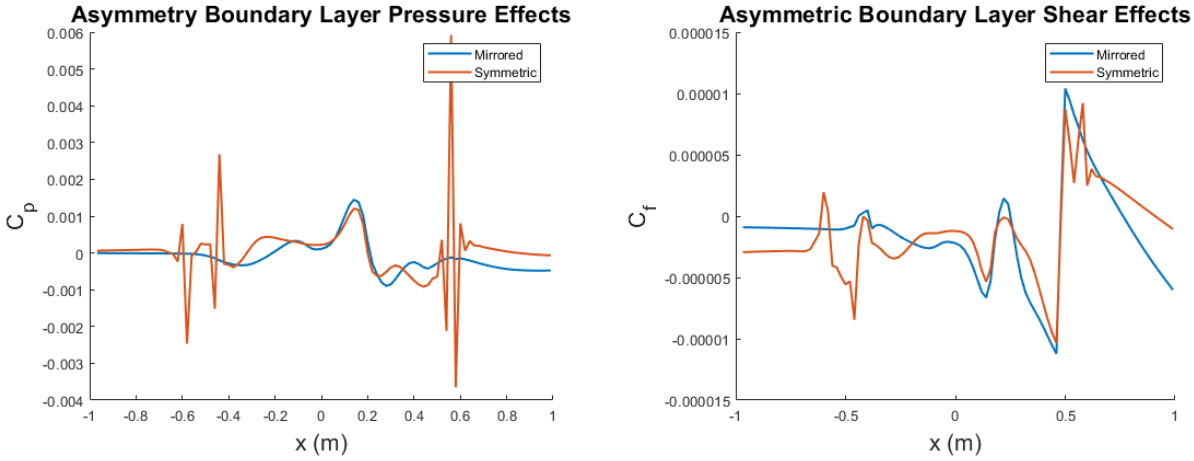

Figure 2.20: Differences in force coefficients due to asymmetry

The size of the incoming boundary layer is then also considered. The size of the boundary layer in the tunnel is unlikely to change significantly between runs or entries which makes this factor less of a risk than the uniformity of the boundary layer, but it is still important to analyze the sensitivity of the bump flow to this variable. The cases considered are all symmetric cases where the inlet face is extruded upstream to locations of 5.5 m, 6 m, and 6.5 m ahead of the bump center. The differences in the pressure and skin friction coefficients are then calculate and plotted in the same way as for the asymmetric cases. Here, the difference are calculated relative to the case where the inlet face is 6 m away from the bump center as this case is most similar in the boundary layer size as measured by experimental data. The results of this analysis are shown in Figure 2.21. We see much more significant magnitudes of difference due to boundary layer size than due to boundary layer non-uniformity. These changes are still very small, but it is recommended that any study of this case should be performed with similar boundary layer sizes as were measured in the experiment. One may also note there exists a peak in the difference in pressure coefficients in the case where the boundary layer is smaller than that of the experiment. This peak occurs at the x-location very near to the area of reattachment on the z = 0 plane. It appears that this case does predict a slightly different location of reattachment than the other two cases. This phenomenon makes the magnitude of this difference relatively large, when the true difference may be more accurately characterized by the difference in the predicted locations of reattachment which is quite small as shown by the interval that this peak occurs on.

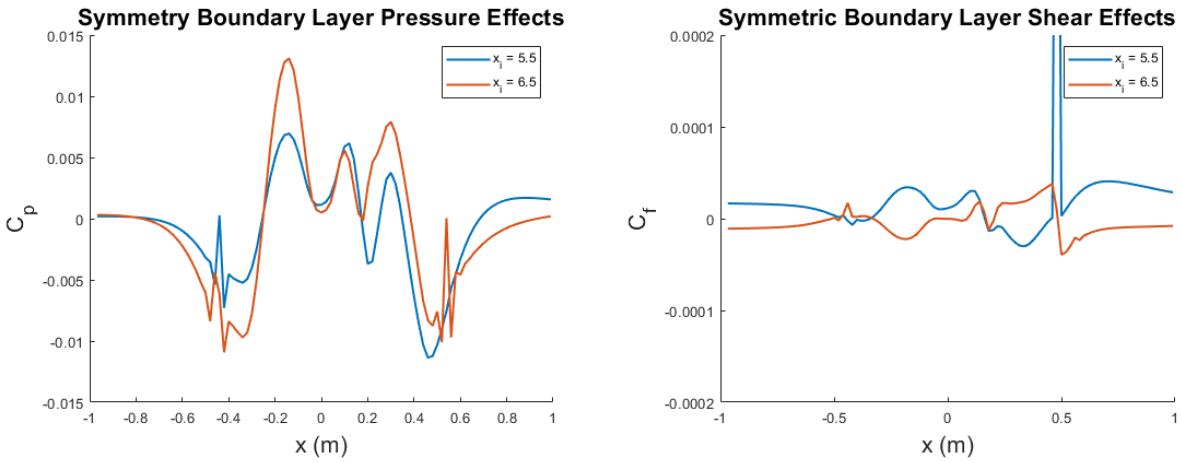

Figure 2.21: Differences in pressure and skin friction coefficients due to asymmetry

2.5 Numerical Solutions for Bump Flow

2.5.1 Fine Mesh Solution

The solutions on the fine grid is used as the most accurate prediction of the flow past the bump in the stability wind tunnel. This solution is obtained with the boundary-layer-matching geometry that was developed in the Section 2.4.1. Plotting the pressure and velocity components in the region around the bump for a slice taken at the z = 0 plane gives an indication of some of the important flow phenomena that are present. Figure 2.22 shows the pressure and all three components of velocity around the bump. In the pressure, we see a region of very high pressures as the flow approaches the bump and slows due to the leading edge curvature in a way similar to the increased pressure along the leading edge of an airfoil. As the flow moves toward the top of the bump, it accelerates, producing high velocities and low pressures over the two areas of curvature at the top. The flow then separates over the leeward side to produce a large region of backflow. For this entirely symmetric geometry, one might expect that the z-component of velocity on the center plane would be zero everywhere, corresponding to a symmetric flow field. However, in these solutions, there exists a significant asymmetry in the flow field despite the enforced symmetry in the computational grid. This asymmetry appears most significantly in the separated region in the wake of the bump as is evidenced by the magnitudes of the z-component of velocity in these regions. It is hypothesized that this geometry exhibits a highly-sensitive bifurcation of the flow field to result in a vortex which is offset from the center plane to one side or another.

Examining flow streamlines can shed further insight into the structure of this flow asymmetry. By seeding the streamlines upstream of the bump, well within the approaching boundary layer, we are able to get a better sense of the flow in the wake. A view showing the stream-

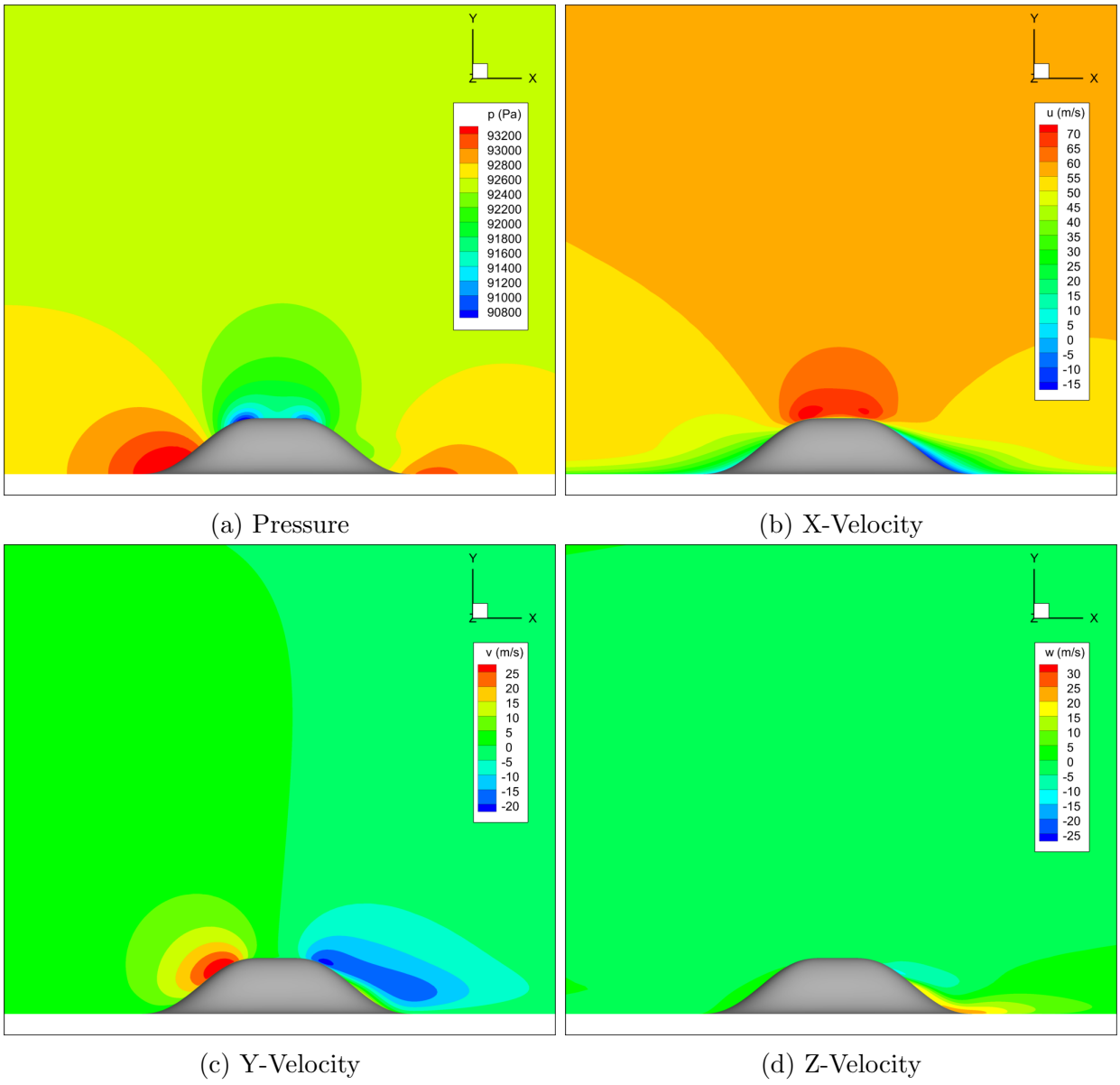

(a) Pressure (b) X-Velocity

(c) Y-Velocity (d) Z-Velocity

Figure 2.22: Flow solutions on center plane

lines' behaviour over the leeward face give an indication of how the flow is behaving in the volume. It is seen that the flow generates a vortex that continues to influence the flow downstream. This vortex causes flow from the port side to be pulled into the leeward side vortex. It is assumed that the direction of this feature in a symmetric domain may only be initiated by the direction of integration determined by the indexing of the structured mesh. As boundary condition information is asymmetrically communicated to the flow in the volume during each iteration, the stable mode of the flow is set to be on one side or another. More analysis is required to determine how stable this flow feature is and whether

it has the potential to change in time.

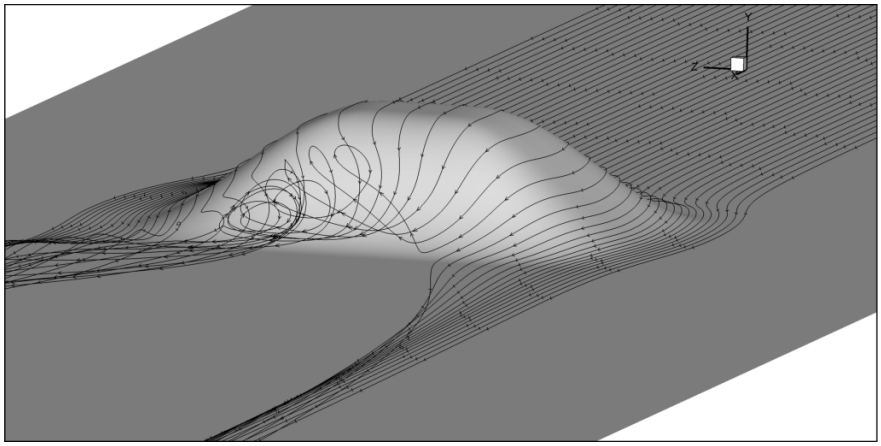

Figure 2.23: Streamlines over the bump surface

This asymmetric feature also has influence on the pressures on the bump surface. This influence is evidenced by plotting three pressure distributions along constant-z lines in the field. These pressures distributions are included in Figure 2.24. It is clear here that there exists significant influence of the asymmetric flow on the pressure in the separated region over the leeward side. The pressure field over the windward face is not much effected by these asymmetries in the wake. The effects of the wake asymmetry on the pressure are seen primarily at the top of the bump and over the leeward side.

Another feature to note from the solution is the shear development over the bump. The shear along the center line is plotted in Figure 2.25. It can be seen that as the flow approaches the bump, the velocity near the surface becomes smaller and the shear stress becomes lower. One may note that at the point where the shear reaches a minimum in this region, it actually becomes negative, suggesting a small region of flow separation. Backflow does indeed occur in this region on a very small scale. Because this feature is very small, it is assumed not to have a significant influence over the rest of the flow field. A full discussion of this feature will be dealt with as this feature is studied as an effect of Reynolds number. It is important to note here that this feature is present on the finest mesh levels as well as the coarsest. It is also seen that the flow exhibits region of high shears along the curvature near the top of the bump. These high values of wall shear impose a narrow restriction on the grid spacing at the wall to satisfy the y^+ ¡ 1 condition for wall-resolved turbulence modeling.

2.5.2 Comparison with Experimental Data

A major goal of the parallel study of this flow computationally and experimentally is the ability to compare directly the results of simulations run and experimental measurements. Early in the experimental design, oil flow visualization was used to identify the flow structures

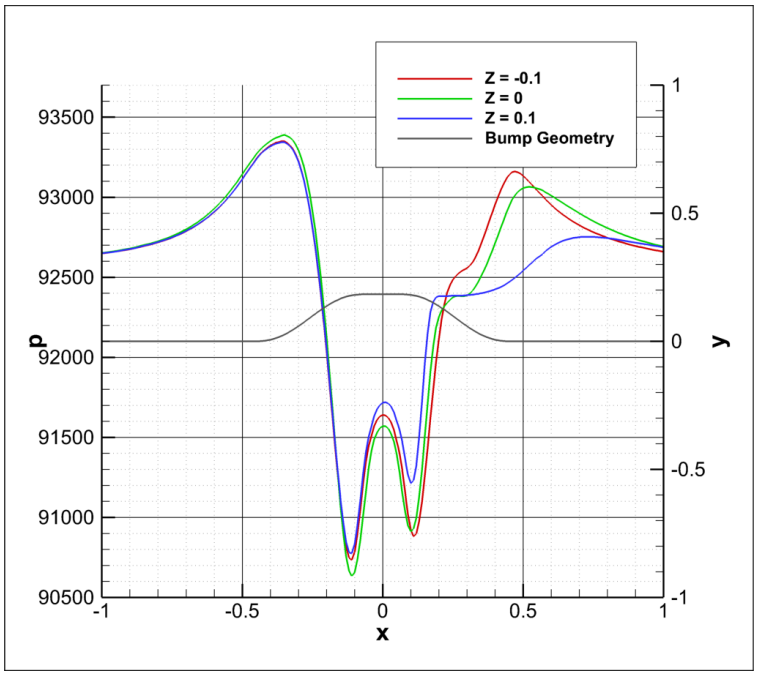

Figure 2.24: Pressures along the bump surface at three z-locations

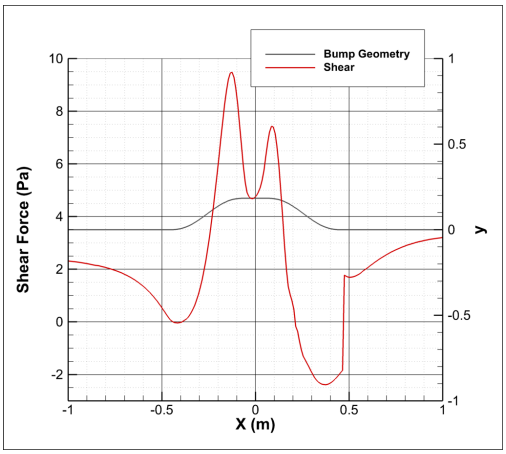

Figure 2.25: Shear along the bump surface

along the surface of the bump. A photograph taken of the oil flow is included in Figure 2.26. The flow in this image is oriented to be moving from left to right. One will immediately notice several important characteristics that can be seen in this image. The first of these is the asymmetric vortex formed over the leeward side of the bump. The vortex seems to form on a particular side of the bump. This observation serves as further evidence toward the idea that there exist two stable modes of this flow over the symmetric geometry as seen in the CFD solutions that have been obtained. Several factors may influence the results seen here. There exist differences in the computationally geometry and the physically tested

geometry due to errors in manufacturing and mounting that have the potential to introduce slight geometric asymmetries. It was observed that the wake flow asymmetry switches sides as the bump is rotated 90 degrees, suggesting that the geometric asymmetries have influence over this feature. The oil flow performed may also be biased by the fact that the bump has been mounted on the tunnel's port side wall, causing gravity to have some influence on the oil's thickness on the bump surface.

Figure 2.26: Photograph of oil flow visualization for bump flow

Another feature that may be noticed from this photograph is the presence of an irregular flow pattern near the bump's leading edge. What is seen in this region may be the same flow separation that is seen in computations of the same flow. The presence of windward separation in the location in the photograph is ambiguous and it does not allow us to confirm the presence of this phenomenon, but it also does not rule out this feature as a potential risk to the bump flow.

Pressure data are also acquired along the surface of the bump geometry. The pressure here is taken relative to ambient atmospheric conditions outside the window and then normalized by the freestream dynamic pressure in the wind tunnel. The free stream dynamic pressure in the test section is measured using several pressure ports in the contraction and settling chamber which can be correlated with the dynamic pressure in the test section in prior calibration studies. Another reference port in the test section is then used as the location from which to consider the reference pressure to ensure consistent normalization of pressure between both computational and experimental data processing. The pressure coefficient at any given port can then be calculated as the difference of the relative pressure measured at that port and the relative pressure measured at the reference port, which is then divided by the freestream dynamic pressure. Pressure coefficients from the CFD solutions can then be calculated in a consistent way by calculating a gauge pressure for each cell relative to the pressure solved for at the location corresponding to the experimental reference port, and then divided by the freestream dynamic pressure as calculated by values taken at the inlet face. These pressure coefficients can then be compared by plotting the values along the

center line of the bump as is done in Figure 2.27.

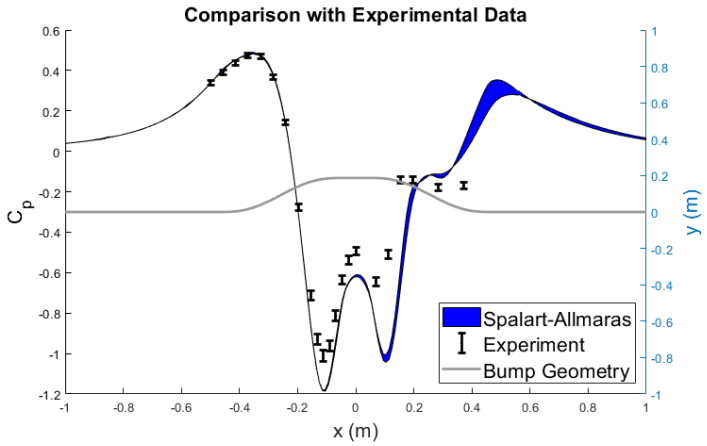

Figure 2.27: Comparison of CFD and experiment pressure coefficients along the center line

Comparison of pressure coefficients shows good agreement as the pressure increases approaching the bump. It seems that the CFD solutions do well in predicting the maximum pressure of the surface. The CFD solutions do not accurately capture the pressure decrease as the flow accelerates over the convex curvature toward the top of the bump. The agreement is worst in the region of separation over the leeward side. Lack of agreement in the separated region is likely due to turbulence modeling imperfections

2.5.3 Influence of RANS Turbulence Model Choice

Solutions are also calculated using the Menter k-ω model in SENSEI. Multiple models are compared to investigate the sensitivity of the solution to the turbulence model that is chosen as well as to perform some initial comparison of the predictive capability for each model for this case. To investigate the influence the model choice may have, regions of separation are plotted using the sign of the x-component of shear stress along the surface in Figure 2.28. It is seen here that there is a dramatic difference in both the size and shape of the separated region predicted by the two models. The Spalart-Allmaras model predicts a more symmetric line of reattachment, while the Menter k-ω-SST model predicts a much less uniform shape. It may also be noticed that the Menter k-ω-SST model does not predict a very large region of separation toward the leading edge as compared to the Spalart-Allmaras model. This separation region appears only in one cell toward the leading edge and also away from the center line of the bump. This creates further uncertainty in the existence of such a feature in the actual experiments.

We may also quantitatively compare the results from the two models by plotting pressure and shear stress along the center line. The center line data is plotted in Figure 2.29. Experimental data is also included for the pressure coefficients. It is seen here that the k-ω model does

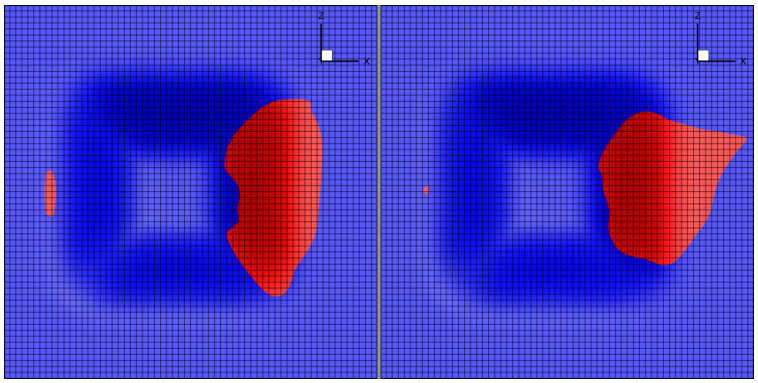

Figure 2.28: Comparison of predicted separated regions predicted with Spalart-Allmaras (left) and Menter k-ω-SST (right) with the flow moving from left to right

seem to offer some improvement over the Spalart-Allmaras model in the ability to predict pressures over the top of the bump as well as in the separated region. The Menter k-ω-SST model shows very different behaviour in the pressure in the separated region as compared to that of the Spalart-Allmaras model. The Spalart-Allmaras model predicts a relatively large peak in the pressure in the region of reattachment which is much less prominent in the k-ω solutions. There is also a large difference in the shear stresses predicted. It is seen that the k-ω model predicts lower shear stresses over the bump's convex curvature with behaviour of this quantity in the separated region being substantially different between the two models.

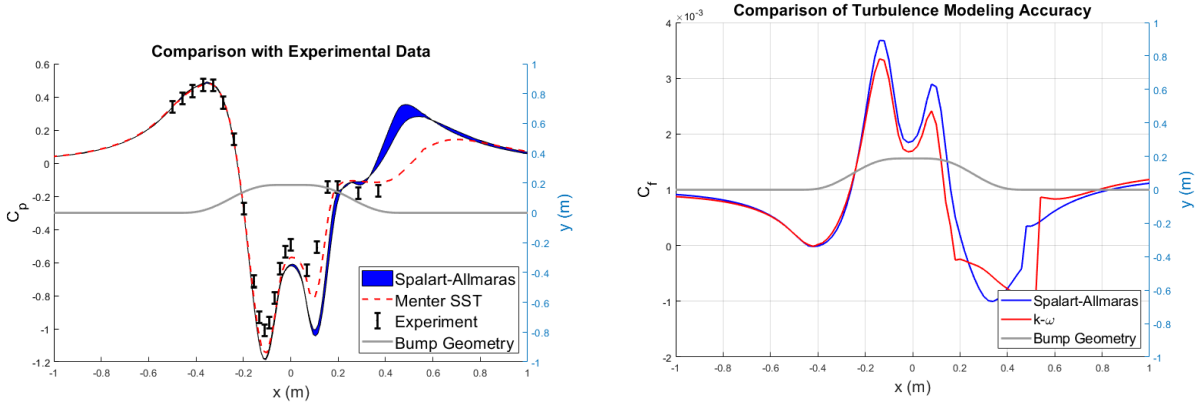

Figure 2.29: Comparison of CFD and experiment pressure and skin friction coefficients along the center line

More experimental data are required to make a definitive conclusion on which model provides better predictive capability for this flow, but it is clear that the CFD solutions are very sensitive to the choice of model, especially in the region of the wake.

2.5.4 Comparison with Fluent Solutions

Solutions are also obtained using ANSYS Fluent on grid level 2 using the Spalart-Allmaras turbulence model. One might expect that as different codes employ different discretizations, schemes, and algorithms, there should be some slight differences in the solutions obtained. Here, the pressure is compared for the solution obtained with fluent as compared that with SENSEI in Figure 2.30. It is seen here that exist many significant differences in the solutions seen here. More investigation is required to identify the source of the discrepancy between these solutions. It is likely that both the difference in the discretizations used and the solution algorithms contribute to the differences seen here. Because both solutions are computed on grid level two, the solutions may be prone to larger discretization errors which will affect the solution differently for different discretizations.

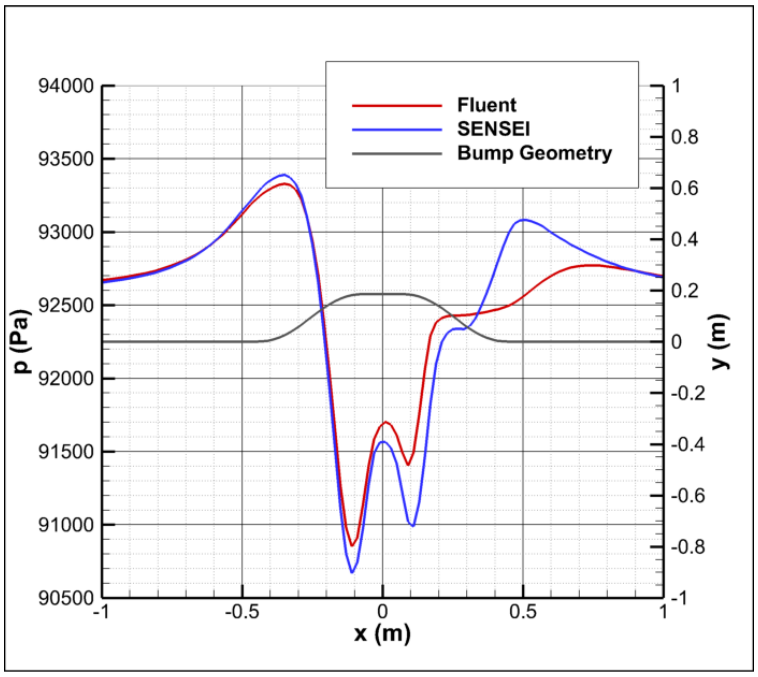

Figure 2.30: Comparison with Fluent solutions using the Spalart-Allmaras model

2.6 Reynolds Number Effects

The current goal of the experiments is to obtain high Reynolds number data. To obtain the highest Reynolds number possible, the size of the bump is chosen to be as large as can be manufactured with reasonable cost and fit into the Stability Wind Tunnel conveniently. The target Reynolds number is calculated with the characteristic length being the bump height and characteristic freestream flow values taken from wind tunnel instrumentation. Because

of annual fluctuations in air temperature and therefore viscosity, the highest Reynolds number that can be safely achieved at every time of the year in the stability wind tunnel with this geometry is 650k. This value is chosen as the target Reynolds number for the experiments, but data are also obtained for a Reynolds number of 325k. Variation in flow characteristics due to Reynolds number are important for the design of the experiment and mitigation of potential risks. Here, solutions for the flow over the bump for five Reynolds number are obtained and directly compared to identify flow field characteristics that may be significantly impacted by this variable. Solutions are obtained on grid level 2 due to the high computational expense of finer mesh solutions.

To change the Reynolds number, the static pressure at the outlet is changed. The height-based Reynolds number is calculated as in Equation 2.12 where ρ_∞ is the reference density, here set to be 1.1271 kg/m^3 in accordance with experimental measurements; V_∞ is the freestream pressure which is varied to achieve the target Re_h; h is the height of the bump which is 0.186944 m; and μ is the reference dynamic viscosity which is specified as 1.78e-5 Pa-s.

$$Re_h = \frac{\rho_\infty V_\infty h}{\mu} \tag{2.12}$$

To target a specific Reynolds number, an isentropic relation is used to solve for the back pressure, p with the assumption that the stagnation pressure, p_0 suffers no losses throughout the test section. This relation uses the ratio of specific heats and the specific gas constant for air, chosen as 1.4 and 287 J/kg/K respectively, as well as the temperature. This relation is shown in Equation 2.13.

$$p = p_0(1 + \frac{\gamma - 1}{2}\frac{V_\infty^2}{\gamma RT})^{-\frac{\gamma}{\gamma - 1}} \tag{2.13}$$

In actuality, stagnation pressure is lost throughout the test section due to aerodynamic forces of the walls and bump model. To find the true freestream velocity in the test section, the reference velocity is taken from the average x-component velocity of a 9-by-9 section of cells at the center of the inlet face. The reference density is taken the same way. The bump height and reference viscosity remain constant for each of the cases. We can then compute the actual solution Reynolds number and compare it to the target. This comparison is performed with results being included in Table 2.4. Because the difference in the target and calculated solution Reynolds number is small, cases will be reported in terms of the target Reynolds number as opposed to that calculated from the solution, with the understanding that there may exist some slight discrepancy.

Table 2.4: Target Reynolds number compared to Reynolds number calculated from solutions.

Target Reynolds Number	Solution Reynolds Number	% Difference
162.5k	157.9k	2.83
325.0k	316.2k	2.72
487.5k	472.9k	2.00
650.0k	640.7k	1.42
812.5k	777.7k	4.29

2.6.1 Windward Separation

After obtaining solutions, the cell-average value of the x-component of velocity may be plotted for the first cell of the wall on which the bump is mounted. The sign of this value allows one to identify potential areas of flow separation. It can be seen from Figure 2.31 that there exists two distinct regions of separation for the flow at this Reynolds number. As one may expect, the flow separates over the leeward side of the bump in a large region of backflow. There also exists a smaller region of separation on the windward side of the bump. This region is generally centered streamwise about the leading edge of the bump. A goal of the current study is to generate a flow that has several of the flow features that are well-suited for turbulence validation studies. An unexpected region of separation ahead of the bump has risk to alter the flow to provide undesirable characteristics that are ill-suited for the purposes of this experiment. The risk of such a feature occurring physically may be ruled out if it can be shown that this feature is either not present at full-scale Reynolds number or that it causes little to no disruption in the important features to be studied.

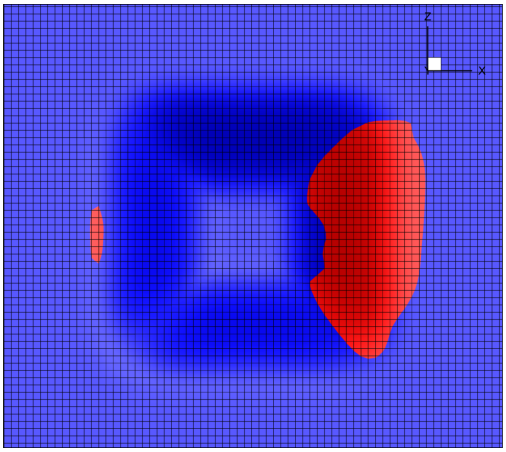

Figure 2.31: The value of the x-component of velocity in the first cell off the wall colored by the sign of its value with red indicating negative shear stress and thus flow separation.

We can study the general size of this feature by plotting a contour line where the x-component of shear along the surface is zero. This contour line is shown in Figure 2.32 for each Reynolds number. The lines seen in this figure indicate a reversal in the direction of the flow and therefore a location at which the flow either separates or reattaches along the surface. Plotting this information for each of the Reynolds numbers shows a distinct trend in the extent of this region in both streamwise and spanwise directions. As the Reynolds number is increased, the region becomes smaller. This trend is an indication that this feature may become decreasingly prominent as the Reynolds number increases. At the target Reynolds number, the region is rather small, while the other Reynolds number tested during the experiment is clearly rather larger and may causes concern for disruptions in the flow field.

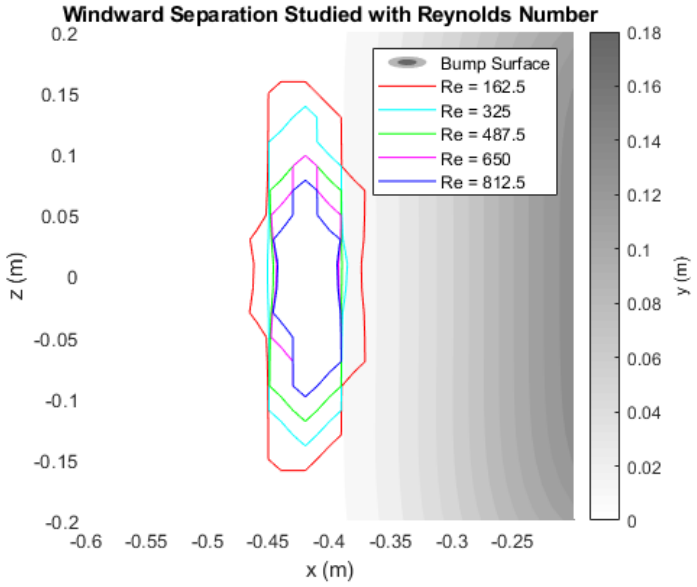

Figure 2.32: Region of separation at the bump's leading edge for each of five Reynolds numbers.

Having studied the extent of the region in the x-dimension and z-dimension, the vertical, or y-direction must also be considered as this may have the most impact on the tendency of features to convect downstream and have important contributions to flow development. To study vertical extent of separation, the boundary layer is plotted at the location X = -.43 m and Z = 0 m (Figure 2.33). This location generally lies in the center of the separated region for each of the five Reynolds numbers considered. When looking at the complete profile, one will notice that boundary layer thickness in this area is generally constant at 300 mm for all Reynolds numbers. The constancy in this value suggests that variations in the upstream development of the boundary layer due to Reynolds numbers becomes negligible in the region of the bump.

The most obvious conclusion that one may draw from the boundary layers in the windward separation region is that it occurs on a very small scale. For the lowest Reynolds number

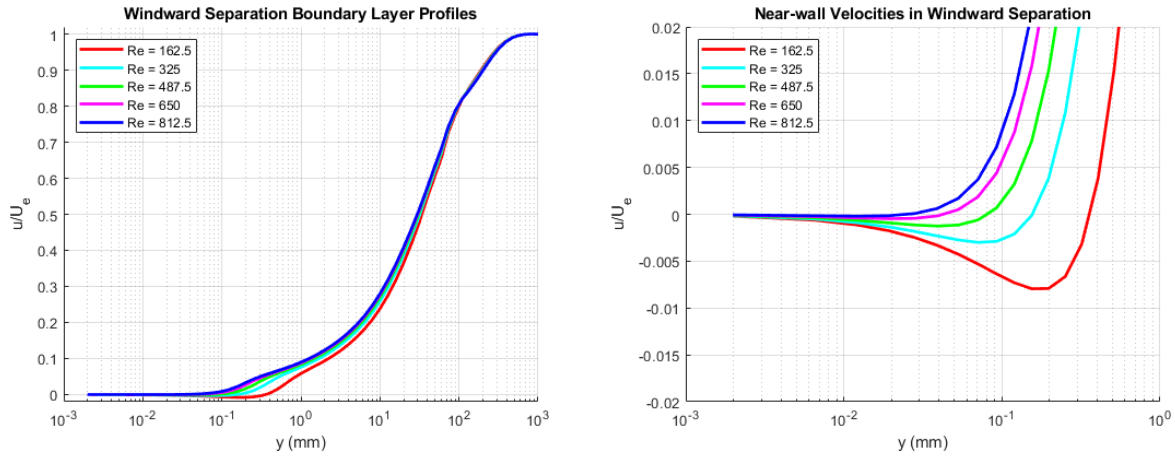

Figure 2.33: Boundary Layer in windward separation region for each of five Reynolds numbers showing a) the entire boundary layer and b) an enlargement of the near-wall region.

considered, this region of separation is about 0.3 mm thick. It also seems to have some impact on the shape of the boundary layer immediately outside of this region as well. For Reynolds numbers above the lowest considered, the vertical extent of separation decreases substantially. At the target Reynolds number of 650k, the region of separation exists only deeply within the viscous sublayer of the turbulent boundary layer. For this reason, we may consider that this geometry, at this Reynolds number is not at risk for large-scale windward separation that has significant downstream effects. For the other Reynolds number for which experimental data have been obtained, there is perhaps some concern of windward separation effects on the flow development over the bump. Because the lower Reynolds numbers for which experimental data are obtained are not the target cases for turbulence modeling validation, it likely does not warrant an alteration to the experimental design.

2.6.2 Leeward Separation

One of the most important goals of studying this geometry both experimentally and computationally is the measurement of the large separation region over the leeward side of the bump. The correct prediction of location where separation begins and where reattachment occurs are intended for use as metrics of model fidelity, and therefore, a knowledge of their sensitivity to Reynolds number is useful. In the same way as was done for windward separation, leeward separation bounds are indicated by the locations at which the the x-component of shear stress changes sign and is therefore zero. These bounds are plotted for the five Reynolds numbers in Figure 2.34. This plot shows that the general extent of the separated region remains relatively constant with Reynolds number.

Furthermore, separation toward the upper corners of the bump occur further upstream for higher Reynolds numbers than for lower Reynolds numbers. Toward the mid-span of the

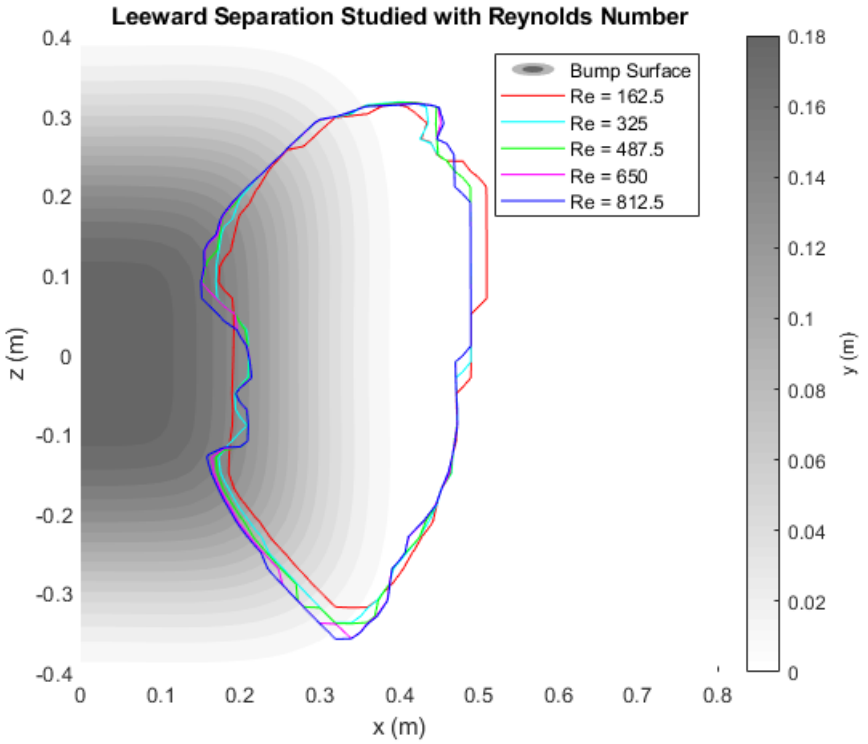

Figure 2.34: Region of separation over the bump's leeward face for each of five Reynolds numbers.

bump, separation occurs later for higher Reynolds numbers. The different behaviour of the separation location toward the center plane and toward the upper corners creates an interesting trend where the shape of the separation line becomes slightly more nonuniform for increasing Reynolds numbers. The area of reattachment remains fairly independent of Reynolds number, however the lower Reynolds numbers do seem to reattach later as viscosity plays a larger role. It is also apparent that spanwise asymmetry exists regardless of the Reynolds number and is likely a feature of the geometry much more so than the regime.

2.6.3 Pressure Distributions

Finally, we will consider how pressure distribution along the bump may change with Reynolds number. The pressure coefficient is calculated along the bump's center line for each Reynolds number. Because the variations due to Reynolds number effects are generally much smaller than changes due to the influence of the bump, the difference in pressure coefficient relative to the lowest Reynolds number is plotted in Figure 2.35. The result shows that, as one may expect, peaks in the pressure are more severe for higher Reynolds numbers. In general, there is little variation in the pressure coefficient. It is interesting to note that the lower Reynolds

numbers do tend to have higher pressure over the leeward side where the flow is separated.

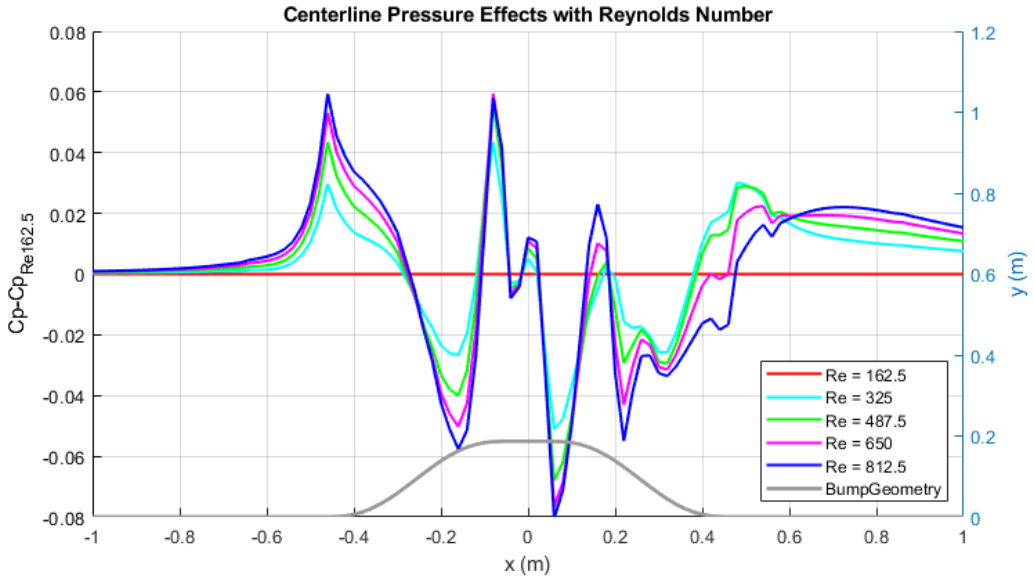

Figure 2.35: Differences in the distribution of pressure over the bump's surface due to Reynolds number effects.

2.7 Conclusions

The results of the preceding studies will be used in the future of the NASA/Virginia Tech Benchmark Experiments to anticipate important flow features and sensitivities, make decisions on locations and types of data that are captured in future experimental entries, and inform future computational studies of the flow. Here, several notable conclusions from the studies performed are summarized. This work sets forward and demonstrates the success of a method of mesh generation for a three-dimensional bump in a wind tunnel. Uncertainty quantification is performed using Richardson extrapolation and a method of iterative error estimation, resulting in estimations of total numerical uncertainty in both pressure and shear stress along the centerline of the bump. A method of matching the inflow boundary layer from experiments has been proposed and found successful. The asymmetric inflow geometry very closely produces the boundary layer integral quantities calculated from experimental data. The degree to which the boundary layer is asymmetric is found to have no significant influence on important features of the flow or on the magnitudes of pressures and shear over the bump surface. The size of the boundary layer is found to have an influence on the magnitude of pressures in some regions and potentially on the extent of the leeward separation region. Solutions are obtained for a Spalart-Allmaras turbulence model and it is shown that the pressures over the convex curvature near the top of the geometry,

as well as in the separated region are not well predicted. The presence of an asymmetric vortex in the wake is confirmed both experimentally and computationally. Results using the Menter k-ω-SST turbulence model more accurately predict the pressure distribution but still show large discrepancies from the experimental data in the separated region. The size and shape of the predicted region of separation are significantly different for the two models considered. Results from running the grid level two in Fluent with the Spalart-Allmaras turbulence model shows significant differences from the same computation using SENSEI. A study of the Reynolds number shows that the flow features are not highly sensitive to the Reynolds number, with the exception of the size of the separated region that is predicted on the windward side.

Acknowledgments

The Virginia Tech team acknowledges the support provided by NASA through an NRA award, grant 80NSSC18M0146, with technical monitor Michael Kegerise, and program manager Mujeeb Malik. This work is accomplished cooperatively with valuable input from a number of collaborators at NASA Langley Research Center including Michael Kegerise, Christopher Rumsey, Catherine McGinley, Luther Jenkins, adn Dan Neuhart. The team also acknowledges the support of the Kevin T. Crofton Department of Aerospace and Ocean Engineering and the Stability Wind Tunnel.

Chapter 3

Discussion and Conclusions

Many factors have the potential to significantly influence the flow past any given geometry. Here, there has been a thorough study of many of these factors using CFD. Code verification is performed on SENSEI via order of accuracy analysis. Numerical error estimation is also performed for surface pressures and shear stresses along the center line of the bump. A method of matching the inflow boundary layer in the test section has been developed and verified. Sensitivity of the flow to both Reynolds number and incoming boundary layer size and uniformity is investigated. Predictive solutions are obtained and analyzed to identify several areas of risk whose sensitivities are then also studied. It is found that the Menter k-ω-SST model produces substantially different results than the Spalart-Allmaras model for quantities in the wake region. It is seen that the Menter k-ω-SST model does display better experimental agreement as well. It is found that there is the potential for separation occurring on the windward face. This risk becomes increasingly problematic at low Reynolds numbers, but at the design Reynolds number, the risk that this feature poses can be ruled out due to its small size. Experimental studies have also found the test section to be subject to boundary layer nonuniformity which has the potential to influence repeatability. An investigation of this phenomena shows the negligible impact that the boundary layer nonuniformity has on both the asymmetry of the separated region on the bump's leeward face, as well as the pressures and shear stresses that are seen on the bump's center line.

3.1 Future Work

There exist many unanswered questions about the flow that is being studied here. Future studies should include an alternate method of matching inflow conditions through a computational modeling of the flow through the contraction. Alternate turbulence models should also be considered and a more thorough study of the influence of turbulence model choice. More codes should also be considered for further verification of solutions with Richardson

extrapolation being performed for each code. Finally, sensitivity of the bump to geometric imperfections in either the bump manufacturing or tunnel mounting should be considered.

Bibliography

[1] Jackson, C. W., Tyson, W. C., and Roy, C. J., "Turbulence Model Implementation and Verification in the SENSEI CFD Code," *AIAA SciTech*, 2019, pp. 2331.

[2] Oberkamp, W.L., S. B., "Assessment Criteria for Computational Fluid Dynamics Model Validation Experiments," *Journal of Verification, Validation, and Uncertainty Quantification*, Vol. 2, No. 3, 2017.

[3] Lowe, K.T., Borgoltz, A., Devenport, W., Fritsch, D., Gargiulo, A., Duetsch-Patel, J., Roy, C. J., Szöke, M., Vishwanathan, V., "Status of the NASA/Virginia Tech Benchmark Experiments for CFD Validation," *AIAA Scitech Forum 2020*, 2020.

[4] Szöke, M., Vishwanathan, V., Fritsch, D., Duetsch-Patel, J., Borgoltz, A., Roy, C. J., Lowe, K. T., and Devenport, W. J., "Computational Fluid Dynamics Simulations of the Virginia Tech Stability Wind Tunnel for Uncertainty Quantification," *AIAA Scitech Forum 2020*, 2020.

[5] Gargiulo, A., L. K. B. A. D. W. F. D. D.-P. J. R. C. J. S. M. V. V., "Examination of Flow Sensitivities in Turbulence Model Validation Experiments," *AIAA Scitech 2020 Forum*, 2020.

[6] Derlaga, J., Phillips, T., and Roy, C., "SENSEI Computational Fluid Dynamics Code: A Case Study in Modern Fortran Software Development," *21st AIAA Computational Fluid Dynamics Conference*, 06 2013.

[7] Spalart, P. and Allmaras, S., "A One-Equation Turbulence Model for Aerodynamic Flows," *Recherch Aerospatiale*, , No. 1, 1994, pp. 5–21.

[8] Menter, F., "Two-Equation Eddy-Viscosity Models for Engineering Applications," *AIAA Journal*, Vol. 32, No. 8, August 1994, pp. 1598–1605.

[9] Weicheng Xue, H. W. and Roy, C. J., "Code Verification for Turbulence Modeling in Parallel SENSEI Accelerated with MPI," *AIAA Scitech 2020 Forum*, 2020.

[10] Oberkampf, W. L. and Roy, C. J., *Verification and validation in scientific computing*, Cambridge University Press, 2010.

[11] Roache, P. J., "Perspective: a method for uniform reporting of grid refinement studies," *Journal of Fluids Engineering*, Vol. 116, 1994.

[12] Spalding, D., "A Single Fomulation for 'Law of the Wall'," *Journal of Applied Mechanics*, Vol. 28, 1961.